Compositional Tuning of Fe/Mn and Fe/Ni Ratios in P3-Type Cathodes Enables High Energy Density Sodium-Ion Batteries

Samriddhi Saxena[a], Neha Dagar[a], Velaga Srihari[b], Karthik Chinnathambi[c], Asish Kumar Das[a], Pratiksha Gami[a], Sonia Deswal[d], Pradeep Kumar[d], Himanshu Kumar Poswal[b], Sunil Kumar[a,*]

[a] *Department of Metallurgical Engineering and Materials Science, Indian Institute of Technology Indore, Simrol, 453552, India*

[b] *High Pressure & Synchrotron Radiation Physics Division, Bhabha Atomic Research Centre, Mumbai 400085, India*

[c] *Micron School of Materials Science and Engineering, Boise State University, Boise, ID 83725, USA*

[d] *School of Physical Sciences, Indian Institute of Technology Mandi, Mandi, 175005, India*

[*] *E-mail: sunil@iiti.ac.in*

ABSTRACT

Layered oxide cathodes are promising candidates for sodium-ion batteries due to their high theoretical capacity and structural tunability. However, irreversible high-voltage redox reactions and structural degradation hinder their practical deployment. In this study, a series of $Na_{0.8}$(Mn–Fe–Ni)O_2 cathodes with systematically varied Fe/Mn and Fe/Ni ratios is investigated to uncover the role of transition metal composition in governing redox behavior, phase transitions, and long-term performance across 2.0–4.0 V and 2.0–4.4 V. Structural analyses reveal that increasing Fe/Mn ratio expands Na-O_2 layer spacing and strengthens TM–O bonds, indicating reduced anionic activity and improved structural stability. $Na_{0.8}Mn_{0.53}Fe_{0.25}Ni_{0.22}O_2$ delivers the highest specific capacity (153 mAh g^{-1}), specific energy (500.3 Wh kg^{-1}), and reversible high-voltage redox activity, retaining 92.6% of its capacity after 100 cycles at 0.2C (2.0–4.4 V). *Operando* Synchrotron X-ray diffraction confirms P3/O3↔P3″/O3 transformations with minimal lattice strain ($\Delta c = \frac{c_{4.4V} - c_{2.0V}}{c_{4.4V}} \times 100\% = -1.81\%$ for O3, +1.00% for P3), contributing to enhanced high-voltage cyclability in $Na_{0.8}Mn_{0.53}Fe_{0.25}Ni_{0.22}O_2$. Meanwhile, $Na_{0.8}Mn_{0.64}Fe_{0.14}Ni_{0.22}O_2$ exhibits exceptional cycling performance (99% retention) in the 2.0–4.0 V range, benefiting from a P3↔P3′ transition. These findings highlight the critical role of Fe/Mn and Fe/Ni tuning in balancing redox reversibility and structural integrity, offering a rational design strategy for high-energy, long-life sodium-ion cathodes.

Keywords: Sodium-ion batteries, Layered oxides, Biphasic P3/O3, Energy Density, *Operando* Synchrotron XRD

1. INTRODUCTION

The rapid growth of the renewable energy sector and the increasing demand for sustainable energy storage systems have intensified the research into cost-effective and resource-abundant battery technologies. Lithium-ion batteries (LIBs) dominate the energy storage market due to their high energy density and optimized performance. However, concerns over lithium resource scarcity and rising costs have driven interest in alternative systems [1]. Among them, sodium-ion batteries (SIBs) have emerged as a promising candidate, offering advantages including lower cost, abundant sodium resources, and compatibility with existing LIB manufacturing infrastructure [2].

A key challenge for SIBs is the development of high-performance cathode materials with energy density and cycling stability comparable to LIB cathodes [3, 4]. Several classes of cathodes for SIBs have been explored, including polyanionic compounds, Prussian blue analogs, and layered transition metal (TM) oxides [5]. Among these, layered transition metal oxides stand out due to their high theoretical capacities, structural tunability, and relatively facile synthesis. These materials, with the general formula Na_xTMO_2 ($0.5 \leq x \leq 1$) (TM = Mn, Ni, Fe, Co, etc.), are analogous to Li-layered oxides and can accommodate a wide range of transition metal combinations [6, 7].

Layered oxides are classified into P2, P3, and O3-type structures depending on the Na^+ coordination environment and TM-O_2 layer stacking sequence [8]. While P2-type materials (e.g., $Na_{2/3}Mn_{2/3}Ni_{1/2}O_2$) offer high rate performance due to larger Na-ion diffusion channels, they often suffer from poor structural reversibility above 4.0 V due to irreversible phase transitions [9, 10]. In contrast, O3-type structures (e.g., $NaMn_{0.5}Ni_{0.5}O_2$) have high specific capacities but are prone to significant volume changes and sluggish kinetics [11]. Recently, P3-type layered oxides have gained attention for offering a balance between structural stability and rate performance [12, 13]. Still, their electrochemical performance, particularly at high voltages, is not fully optimized.

Compositional tuning has been widely employed to improve the performance of layered transition metal cathodes, enabling control over redox activity, structural reversibility, and long-term cyclability [6, 14, 15]. In particular, Mn–Ni–Fe pseudo-ternary systems are promising due to the complementary roles of each element. Mn provides structural stability, Ni contributes to higher capacity via Ni^{2+}/Ni^{4+} redox, and Fe offers cost effectiveness and high-voltage redox activity (~ 4 V). Numerous studies have reported promising results from Fe-

substituted compositions such as $NaMn_{0.625}Fe_{0.125}Ni_{0.250}O_2$, $Na_{2/3}Ni_{1/3}Mn_{7/12}Fe_{1/12}O_2$, $NaNi_{1/3}Fe_{1/3}Mn_{1/3}O_2$, and $Na_{2/3}[Ni_{1/4}Mn_{7/12}Fe_{1/6}]O_2$, showing improved voltage profiles, phase stability, and moderate to high capacities [16-18].

Beyond enhancing structural stability, Fe substitution has also been linked to the modulation of redox pathways. Fe^{3+}/Fe^{4+} redox, around 4.0 V, has been shown to delay or suppress the onset of anionic (oxygen) redox, a mechanism often activated above 4.1 V and known to contribute extra capacity [19]. While anionic redox has been reported in several Na-layered systems such as $Na_{0.67}Fe_{0.5}Mn_{0.5}O_2$, $Na_{0.67}Mn_{0.72}Mg_{0.28}O_2$, and $Na_{0.67}Ni_{0.33}Mn_{0.67}O_2$, [20-23] it is typically accompanied by O_2 gas evolution, irreversible phase transitions (e.g., P2 to Z/O2 or OP4), large voltage hysteresis, and rapid capacity fading due to structural collapse [22, 24-26]. Therefore, tuning TM ratios to promote controlled redox behavior, particularly involving Fe, offers a promising strategy for stabilizing high-voltage performance.

Although ternary Na(Mn-Fe-Ni)O_2 compositions have been widely investigated, most studies have limited their scope to a single compositional axis, typically varying Fe or Ni content while keeping the others constant. For instance, Hwang et al. prepared a series of O3-type layered $Na[Ni_{0.75-x}Fe_xMn_{0.25}]O_2$ (x = 0.4, 0.45, 0.5, and 0.55) oxides with fixed Mn (25%). Ni/Fe ratio of 0.5 was identified as optimal for achieving improved cyclability and rate performance in the 1.5 – 3.9 V range [27]. Similarly, Liang et al. investigated a series of P2-type $Na_{0.67}Ni_xFe_{0.52-x}Mn_{0.48}O_2$ materials with varying Ni/Fe ratios, identifying $Na_{0.67}Ni_{0.22}Fe_{0.30}Mn_{0.48}O_2$ as the most promising composition, which delivered an initial discharge capacity of 174.2 mAh g^{-1} and a 72.7 % capacity retention after 300 cycles [28]. However, to our knowledge, the simultaneous effects of varying Fe/Mn and Fe/Ni ratios, particularly in P3-type frameworks, have not been systematically explored.

A recent study on the $Na_{0.8}$(Mn-Fe-Ni)O_2 pseudo-ternary system presented detailed structural and electrochemical characterization of compositions synthesized at 700 °C, 800 °C, 900 °C, and 1000 °C with a focus on evaluating the effect of Mn/Ni ratio variation while maintaining a fixed Fe content [29]. Among the reported compositions, P2-type $Na_{0.8}Mn_{0.64}Fe_{0.14}Ni_{0.22}O_2$, synthesized at 800 °C, demonstrates a balance between capacity, cyclability, and rate performance. In this work, the influence of Fe/Mn and Fe/Ni ratios is examined on the structural and electrochemical behavior of P3-type layered oxides. Five compositions, centered around $Na_{0.8}Mn_{0.64}Fe_{0.14}Ni_{0.22}O_2$, are selected strategically so as to represent variations along Fe/Mn and Fe/Ni ratio lines (Fig. S1 (Supplementary Material)). The compositions are as

follows: MFN-1 – $Na_{0.8}Mn_{0.75}Fe_{0.03}Ni_{0.22}O_2$, MFN-2 – $Na_{0.8}Mn_{0.64}Fe_{0.03}Ni_{0.33}O_2$, MFN-3 – $Na_{0.8}Mn_{0.64}Fe_{0.14}Ni_{0.22}O_2$, MFN-4 – $Na_{0.8}Mn_{0.64}Fe_{0.25}Ni_{0.11}O_2$, and MFN-5 – $Na_{0.8}Mn_{0.53}Fe_{0.25}Ni_{0.22}O_2$. Among these, compositions MFN-1, 3, and 5 are located along a constant Ni line with varying Fe/Mn ratios, while MFN-2, 3, and 4 lie along a constant Mn line with varying Fe/Ni ratios. All samples crystallize predominantly in a layered P3-type structure. Structural analysis indicates that increasing the Fe/Mn and Fe/Ni ratios leads to a systematic expansion of the Na-layer spacing and a concurrent contraction of the TM layer. Additionally, Mn–O bond is shortened with increasing Fe/Mn ratio, indicative of stronger TM–O interactions. Operando synchrotron XRD reveals reversible P3/O3 ↔ P3″/O3 transitions in MFN-5 with minimal lattice strain, highlighting its superior structural stability at high voltages. Electrochemically, MFN-5 delivers the highest specific discharge capacity of 153 mAh g^{-1}, and a specific energy of ~ 500 Wh kg^{-1} in the 2.0 – 4.4 V range. Differential capacity profiles of MFN-5 reveal two distinct and reversible high-voltage redox peaks at 4.16 V and 4.23 V. In contrast, MFN-3 excels in the narrow voltage range, retaining 99% of its capacity after 100 cycles. This superior stability is attributed to a reversible P3 → P3′ phase transition and a delayed onset of oxygen redox, resulting in reduced structural strain and highly reversible Ni/Fe redox behavior. Together, these findings demonstrate that rational tuning of Fe/Mn and Fe/Ni ratios enables precise control over redox mechanisms and structural evolution, providing a robust framework for the design of high-energy, long-life sodium-ion cathodes.

2. EXPERIMENTAL SECTION

2.1. Materials Preparation

A series of MFN cathode compositions was synthesized via a wet chemical approach. Stoichiometric quantities of Na_2CO_3 (SRL, 99.9%), manganese(II) acetate tetrahydrate ($C_4H_6MnO_4{\cdot}4H_2O$, Sigma-Aldrich, > 99%), iron(III) nitrate nonahydrate ($Fe(NO_3)_3{\cdot}9H_2O$, Rankem, 98%), and nickel(II) acetate tetrahydrate ($C_4H_6NiO_4{\cdot}4H_2O$, Sigma-Aldrich, 98%) were dissolved in deionized water. This solution was stirred for 8 h, followed by the addition of citric acid ($C_6H_8O_7$) as a chelating agent and ethylene glycol ($C_2H_6O_2$) to promote gelation. The mixture was further stirred until homogenized and subsequently heated to initiate gel formation. The obtained gel was dried and subjected to a two-step thermal treatment, an initial heat treatment at 550 °C for 12 h and subsequent calcination at 650 °C for 12 h in ambient air using a muffle furnace. The calcined powders were naturally cooled to room temperature and stored in an argon-filled glove box to avoid moisture-induced degradation.

2.2. Materials Characterization

The elemental composition of the synthesized cathode powders was determined by inductively coupled plasma optical emission spectrometry (ICP-OES, Agilent 5800). Crystallographic phase identification was carried out using X-ray diffraction (XRD) with Cu-Kα radiation on an Empyrean diffractometer (Malvern Panalytical). XRD data were collected over a 2θ range of 10°–70° with a step size of 0.01° and analyzed using Rietveld refinement via Topas academic software (version 6) [30]. Mn, Fe, and Ni K-edge extended X-ray absorption fine structure (EXAFS) measurements were conducted at the BL-9 scanning EXAFS beamline at the Indus-2 Synchrotron radiation facility (2.5 GeV, 150 mA), at the Raja Ramanna Centre for Advanced Technology (RRCAT), Indore, India. The morphology of the cathode particles was observed using field emission scanning electron microscopy (FESEM, JEOL-7610), and elemental mapping was performed via energy dispersive X-ray spectroscopy (EDS). Transmission electron microscopy (TEM) imaging was carried out using a JEOL-2100 microscope, with samples drop-cast onto carbon-coated Cu grids. Elemental oxidation states were analyzed by X-ray photoelectron spectroscopy (XPS) using a Thermo Fisher Scientific instrument equipped with an Al Kα X-ray source (1486.6 eV).

2.3. Electrochemical Measurements

The cathodes were fabricated by preparing a slurry consisting of 75 wt% active material, 10 wt% Ketjen black, and 15 wt% polyvinylidene fluoride (PVDF) binder dispersed in N-methyl-2-pyrrolidone (NMP). The slurry was coated onto aluminum foil and dried under vacuum. The dried films were punched into 14 mm discs, with an active material loading between 3 and 4 mg cm^{-2}. Coin-type (CR2032) cells were assembled in an argon-filled glove box, using sodium metal as the counter/reference electrode. For full-cells, hard carbon was used as the anode material, prepared by mixing 80 wt% hard carbon, 10 wt% Ketjen black, and 10 wt% PVDF, followed by coating onto aluminum foil. Before cell assembly, the hard carbon electrode was cycled for two cycles in a half-cell configuration with sodium metal. A 1 M solution of $NaClO_4$ in a 1:1 volumetric mixture of ethylene carbonate (EC) and propylene carbonate (PC) was used as the electrolyte, with Whatman GF/D glass fiber as the separator.

Galvanostatic charge–discharge (GCD) profiles at various current densities were recorded using a Neware CT-4008T battery testing system. The same system was employed for galvanostatic intermittent titration technique (GITT) experiments to estimate Na^+ diffusion coefficients. *Operando* Synchrotron XRD measurements were conducted at beamline BL-11

of the Indus-2 Synchrotron (RRCAT) to monitor structural evolution during cycling, using a beam energy of 2.5 GeV (λ = 0.7388 Å). Coin cells for *operando* studies were modified by drilling 5 mm holes in the casing to enable X-ray transmission, which were subsequently sealed with Kapton tape to isolate the internal cell environment from ambient air.

3. RESULTS AND DISCUSSION

3.1. Structural characterization

Table S1 (Supplementary Material) lists the elemental ratios of the MFN samples obtained from Inductively coupled plasma optical emission spectroscopy (ICP-OES) analysis. The calculated compositions closely match the nominal values, confirming that the target stoichiometry was achieved. Fig. S2 (Supplementary Material) shows the room temperature X-ray diffraction (XRD) patterns for MFN samples calcined at 650 °C. All diffraction peaks align with the Bragg positions of the layered P3 and O3 phases, and no impurity peaks are observed. Notably, the patterns reveal a strong preference for the P3 phase across all samples, which is expected given that the P3 phase typically forms at lower calcination temperatures [14]. The MFN-5 sample with the highest Fe/Mn ratio ($Na_{0.8}Mn_{0.53}Fe_{0.25}Ni_{0.22}O_2$) exhibits a P3/O3 biphasic structure. This is evident from the intensity ratios of the (104) and (105) peaks, where the (104) peak is noticeably more intense than the (105) peak in the O3 phase, while the (105) peak is stronger in the P3 phase. These observations are consistent with prior studies [31]. Additionally, previous reports suggest that increasing Fe content promotes O3 phase formation due to the d^5 configuration of Fe^{3+}, which prefers the octahedral coordination [29, 32].

Based on peak intensity ratios, the fractions of P3 and O3 phases are estimated to be ~ 75% and 25%, respectively [33]. The Rietveld refinement of the XRD data shows that the P3 and O3 phases correspond to the $R3m$, and $R\bar{3}m$ space groups, respectively (Fig. 1). Phase quantification reveals that MFN-5 consists of ~ 76% P3 and ~ 24% O3 phases, which align closely with the values estimated by the peak intensity ratio (Fig. 1(f)). The lattice parameters obtained from the refinement are presented in Table 1.

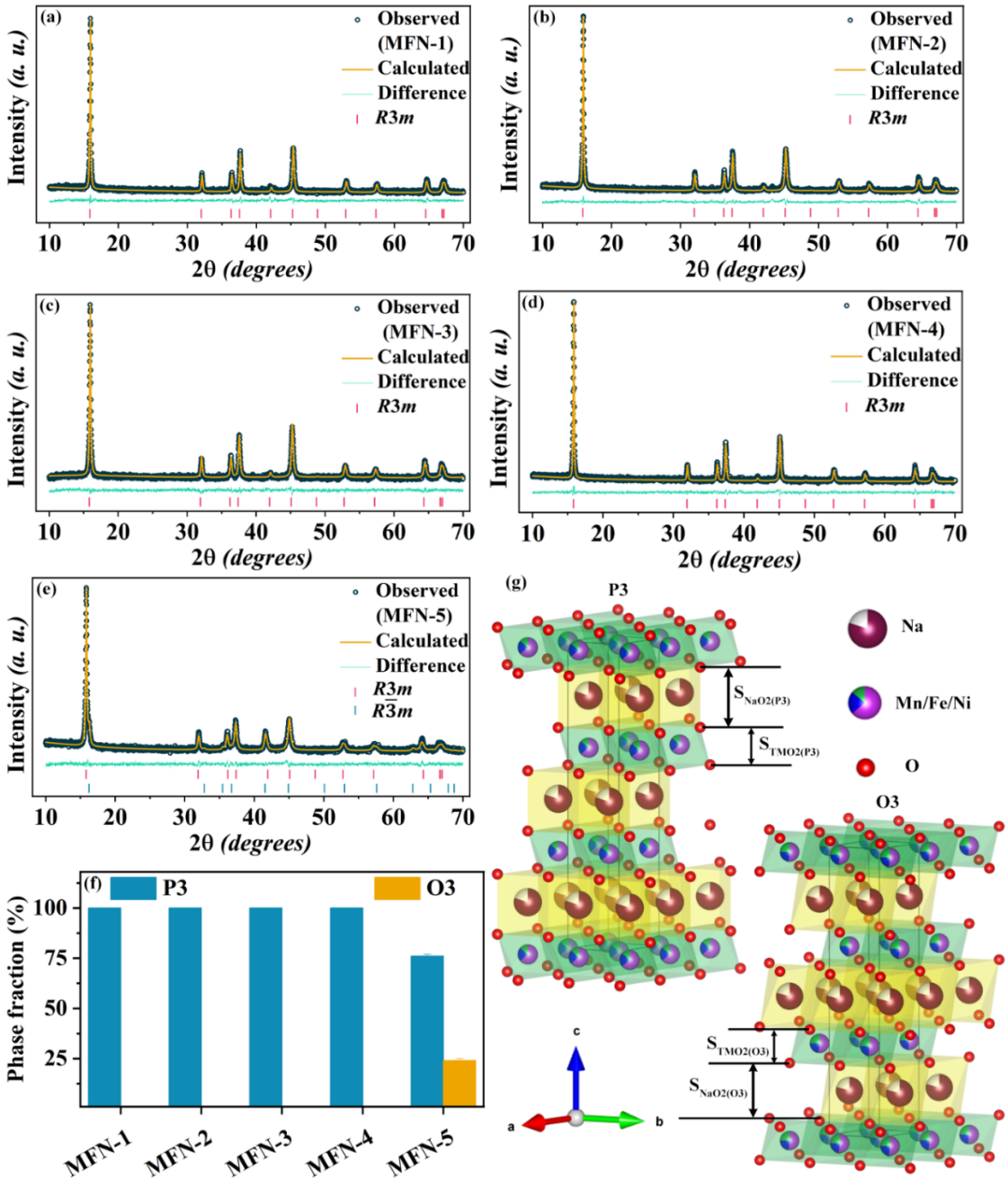

Fig. 1. (a-e) Rietveld refinement profile of XRD data for MFN samples, (f) Graph showing phase percentage of P3 and O3 phases in MFN samples, and (g) Schematic of P3 and O3 crystal structures.

Table 1. Lattice parameters of MFN samples obtained by the Rietveld refinement of XRD data.

Sample	***Phase***	***a* (Å)**	***c* (Å)**	***V* (Å^3)**	***R_{wp}, R_{exp}, R_p, GOF***
MFN-1	P3: 100	2.8850 ± 0.0001	16.769 ± 0.001	120.87 ± 0.02	2.3986, 2.0133, 1.8986, 1.1913

MFN-2	P3: 100	2.8907 ± 0.0001	16.771 ± 0.001	121.37 ± 0.01	2.4848, 2.0793, 1.9599, 1.1950
MFN-3	P3: 100	2.8946 ± 0.0001	16.789 ± 0.001	121.77 ± 0.03	2.7843, 2.5042, 2.2369, 1.1118
MFN-4	P3: 100	2.8976 ± 0.00002	16.807 ± 0.001	122.20 ± 0.01	2.1635, 1.8497 1.6856, 1.1696
MFN-5	P3: 76 ± 1	2.9059 ± 0.0002	16.804 ± 0.003	122.91 ± 0.03	2.5548, 2.3446, 2.0155, 1.0896
	O3: 24 ± 1	2.9573 ± 0.0005	16.373 ± 0.004	124.01 ± 0.05	

Across constant Ni content, a progressive increase in the *c* parameter is observed with increasing Fe/Mn ratios. A similar trend is evident at a fixed Mn content, where increasing the Fe/Ni ratio also results in lattice elongation along the *c*-axis. These observations suggest that Fe incorporation expands the unit cell, while higher Ni content exerts a contracting effect. Notably, this behavior deviates from the expected trend based on ionic radii, as Ni^{2+} (0.69 Å) is larger than Fe^{3+} (0.55 Å), Mn^{3+} (0.58 Å), and Mn^{4+} (0.53 Å). This implies that factors beyond ion size, such as electronic structure, local coordination environment, or bonding characteristics, have a more significant role in determining lattice parameters [34]. The structural parameters obtained from the refinement are provided in Tables S2-S6 (Supplementary Material). A visual of the variation in the *c* parameter is provided by an overlaid XRD plot for better comparison of the (003) peak of the P3 in Fig. S3 (Supplementary Material). The *c* parameter of MFN-3 is higher than that of MFN-1 and MFN-2; however, its peak position appears slightly shifted due to a minor *sample displacement* error. A similar displacement is observed for MFN-5, resulting in its peak appearing at a higher 2θ value compared to MFN-4.

The crystal structures of the P3 and O3 phases were modeled based on Rietveld-refined parameters and visualized using VESTA, as presented in Fig. 1(g). The transition metal layer spacing (S_{TMO_2}) and the sodium layer spacing (S_{NaO_2}) in the P3 and O3 phases were calculated using the following equations:

$$S_{TMO_2}(\mathrm{P3}) = \frac{2c}{3}(2z_{O1} - z_{O2}) \qquad (1)$$

$$S_{NaO_2}(\mathrm{P3}) = c(z_{O2} - z_{O1}) \quad (2)$$

$$S_{TMO_2}(\mathrm{O3}) = 2c\left(\frac{1}{3} - z\right) \quad (3)$$

$$S_{NaO_2}(\mathrm{O3}) = \frac{c}{3} - S_{TMO_2}(\mathrm{O3}) \quad (4)$$

Here, z and c denote the fractional coordinate z of the oxygen ions and the c parameter, respectively. The calculated interlayer spacings are summarized in Table S7 (Supplementary Material). The Na layer spacing of the P3 phase increases from 3.3203 Å for MFN-1 to 3.4280 Å for MFN-5, and the TM layer spacing decreases from 2.2694 Å to 2.1713 Å. Therefore, increasing the Fe/Mn ratio results in an expanded Na layer. Similarly, increasing the Fe/Ni ratio (at constant Mn) also enlarges the Na layer spacing, though the change is more subtle between MFN-3 and MFN-4.

The reduction in TM layer spacing correlates with shortened TM-O_2 bond lengths, indicating stronger TM-O_2 interactions. This contraction of the TM–O layers with increasing Fe/Mn and Fe/Ni ratios was further supported by the fitting of Extended X-ray absorption fine structure (EXAFS) data obtained at the Mn K-edge (Fig. S4 (Supplementary Material)). The corresponding Fourier transforms display two prominent peaks, representing the average length of the Mn-O bond of the first shell and the average length of the Mn-TM bond of the second shell, respectively. Along the increasing Fe/Ni ratio, Mn–O distances decrease from 1.94 Å in MFN-2 to 1.90 Å in MFN-4, while a similar contraction is observed from 1.96 Å in MFN-1 to 1.91 Å in MFN-3 along the increasing Fe/Mn ratio. This enhanced bonding can suppress oxygen redox activity at high voltages. In this regard, MFN-5 with the shortest S_{TMO_2} of 2.17 Å is expected to have suppressed anionic redox activity and relatively stable performance when cycled beyond 4 V. Moreover, the broader Na layer spacing weakens the Na-O_2 electrostatic interaction and facilitates wider diffusion channels, thereby promoting faster Na^+ transport during charge/discharge.

The morphology of the MFN series was examined via field emission scanning electron microscopy (FESEM) (Fig. 2), revealing a dominant presence of spheroidal particles in the nanometer size range. The spheroid morphology of the particles at lower calcination temperatures is primarily driven by the system's tendency to minimize surface energy. The *{001}* surfaces of layered oxides, which have lower surface energies compared to the (*h00*), (*0k0*), and (*hk0*) planes, are exposed during crystal growth [35]. The smaller particle size at

lower calcination temperatures restricts the growth of anisotropic features, suppressing the formation of sharp edges or elongated facets. Instead, the system favors a more isotropic growth, resulting in the formation of rounded particles that minimize the total surface area and, consequently, the overall surface energy of the system.

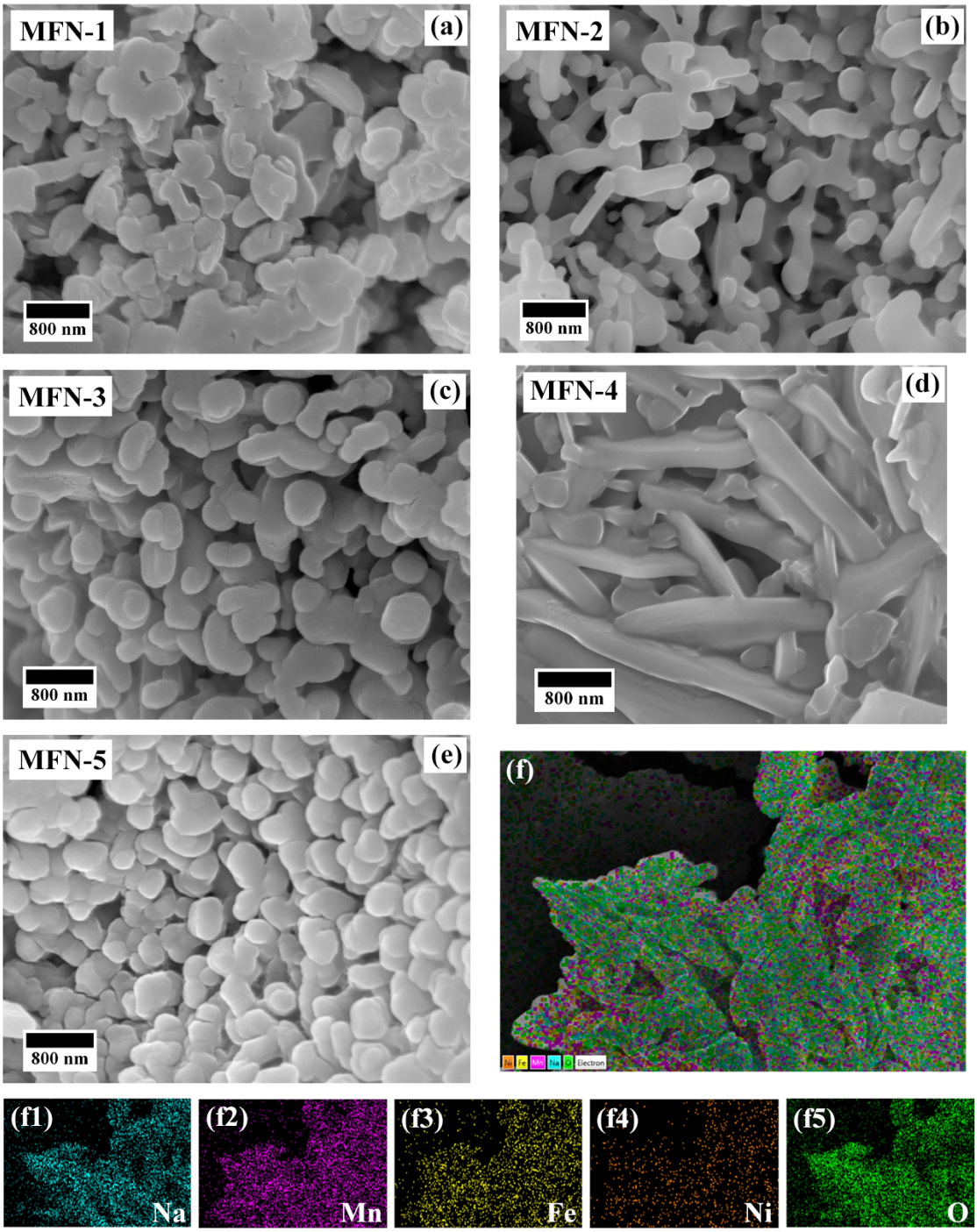

Fig. 2. (a-e) SEM micrographs of MFN samples calcined at 650 °C, (f) Average particle sizes of the samples, and (g) EDS map of MFN-4 showing uniform distribution of all the elements.

A cathode material composed of smaller, well-dispersed particles offers shorter Na^+ diffusion paths, which enhances the performance, particularly at high discharge rates. While the influence of particle size may be negligible at low C-rates (~ 0.1 C), it becomes a critical factor at elevated rates where Na-ion diffusion in the solid phase is the rate-limiting step. Along the constant Mn line, MFN-2, with the lowest Fe/Ni ratio, shows small, partially joined spheroids, likely due to high Ni content, where the slower diffusion of Ni may the formation of defined features within the given synthesis time. Increasing Fe and reducing Ni in MFN-3 produces relatively larger spheroids, while MFN-4, with the highest Fe and lowest Ni, displays a mixed morphology of spheroids and plate-like particles. The higher Fe content could modify the surface energy, favoring anisotropic growth and thereby promoting preferential growth of the {001} surfaces, leading to plate-like features. Along the constant Ni line, a lower Fe/Mn ratio in MFN-1 again yields partially evolved spheroids, while increasing the Fe/Mn ratio in MFN-3 and MFN-5 leads to larger average particle sizes. Spheroidal particles with isotropic orientations allow Na-ion transport in multiple directions, supporting efficient ion movement across the particle. As morphology shifts to plate-like structures, limited lateral surface area and dominance of *{001}* surfaces limit Na-ion diffusion, which increases polarization and reduces rate capability.

The average particle sizes of the spheroids in MFN-1 (343 ± 26 nm), MFN-2 (312 ± 13 nm), MFN-3 (321 ± 16 nm), MFN-4 (355 ± 21 nm), and MFN-5 (347 ± 19 nm) were determined from the SEM images. MFN-4 exhibits a broader particle size distribution and a mixed morphology, consisting of spheroidal particles together with thin plate-like structures of average lateral size 1.9 ± 0.2 μm and thickness ~230 ± 6 nm. Elemental mappings (Fig. 2 (f)) confirm that all elements in MFN-4 are evenly distributed throughout the sample, indicating that the observed morphological variation arises from the material composition itself, rather than from phase or elemental segregation. The broad size distribution observed in MFN-4, including both spheroid and plate-like structures, can complicate the electrode fabrication process and can result in uneven electrochemical activity and reduced overall cell performance.

The local structure of the samples was further investigated using transmission electron microscopy (TEM). Fig. 3(a-e) displays the bright-field images, high-resolution TEM (HRTEM) micrographs, and SAED patterns for MFN-2, while Fig. 3(f-h) presents corresponding results for MFN-5. The HRTEM image reveals well-defined lattice fringes with an interlayer spacing of 5.59 Å, corresponding to the (003) planes of the P3-type layered framework in MFN-2, in agreement with the results of XRD refinement.

The SAED patterns acquired along the [211] zone axis (Fig. 3 (d, g)) show distinct diffraction spots indexed to the $(01\bar{1})$, $(10\bar{2})$, and $(1\bar{1}\bar{1})$ planes of the P3-phase, confirming the layered structure with R3*m* symmetry. Additionally, faint reflections appear between the main diffraction spots in both MFN-2 and MFN-5, indicative of a superlattice structure associated with cation ordering [36]. In MFN-2, the superstructure adopts a $(2\sqrt{3} \times 2\sqrt{3})$-R30° arrangement, while MFN-5 shows a $(\sqrt{3} \times \sqrt{3})$-R30° ordering configuration [9, 37]. The differences in the superstructure types between the two samples are likely linked to variations in Fe concentration. The incorporation of Fe^{3+} can influence the local cation arrangement, stabilizing different ordering configurations.

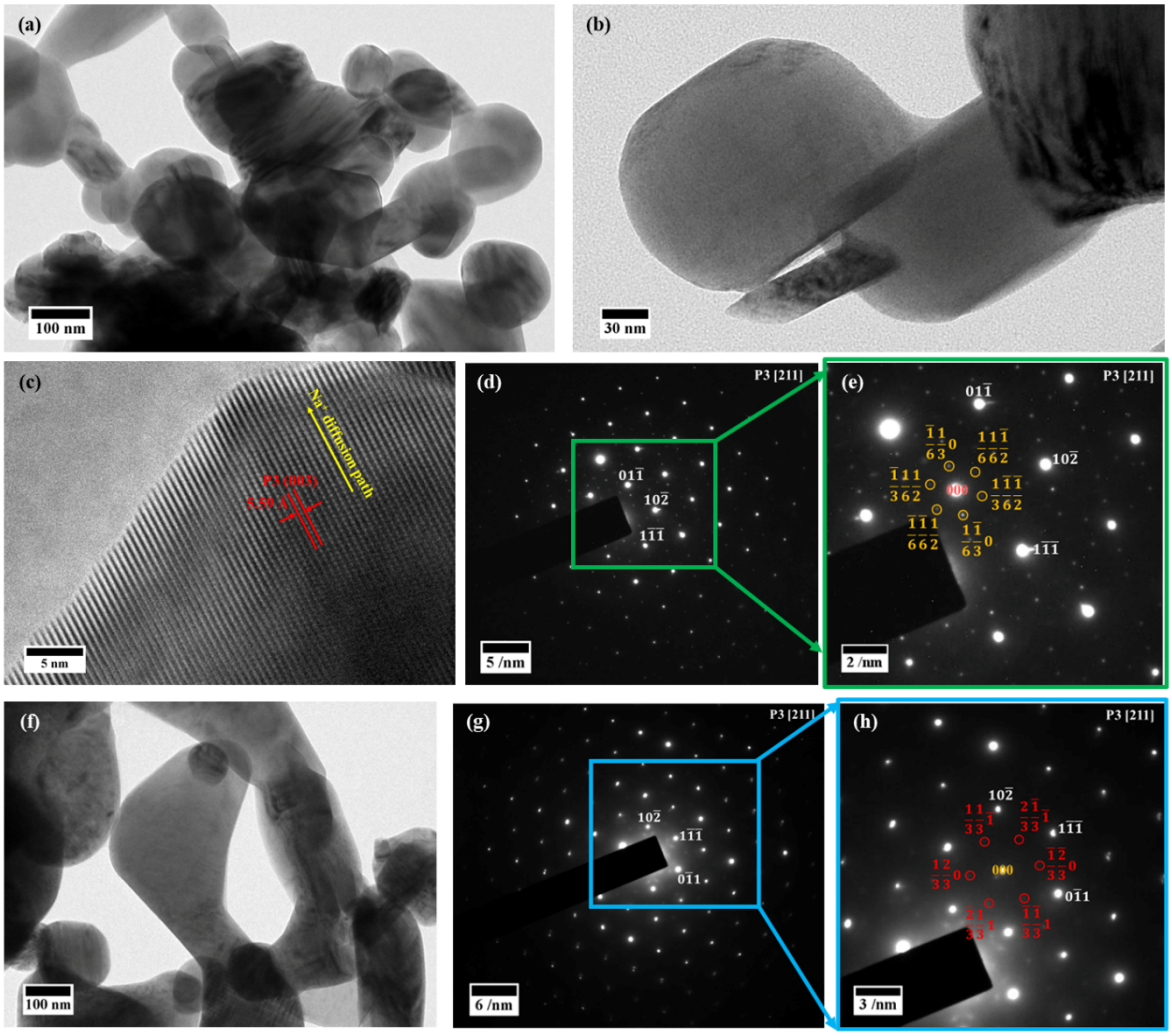

Fig. 3. (a,b) Bright-field HRTEM images of MFN-2, (c) Atomic resolution image of MFN-2, (d) SAED pattern of MFN-2 captured along the [211] zone-axis, (e) A magnified image showing the superlattice ordering peaks in MFN-2, (f) Bright-field HRTEM image of MFN-5,

(g) SAED pattern of MFN-5 captured along the [211] zone-axis, and (h) A magnified image showing the superlattice spots in MFN-5.

The oxidation states of Mn, Fe, and Ni in the MFN series were elucidated using a combination of X-ray photoelectron spectroscopy (XPS) and X-ray absorption spectroscopy (XAS). XPS was first employed to determine the surface oxidation states of Mn, Fe, and Ni, and the corresponding high-resolution XPS spectra of Mn2p, Fe2p, and Ni2p are shown in Fig. 4 (a-c). The Mn 2p spectrum exhibits two doublets corresponding to Mn^{3+} ($2p_{3/2}$ ~ 641.2 eV; $2p_{1/2}$ ~ 651.9 eV) and Mn^{4+} ($2p_{3/2}$ ~ 642.6 eV; $2p_{1/2}$ ~ 653.7 eV) [38, 39]. The estimated Mn^{3+}/Mn^{4+} ratios for all samples are provided in Table S8 (Supplementary Material). A progressive decrease in the Mn^{3+}/Mn^{4+} ratio is observed from MFN-1 to MFN-5 along the increasing Fe/Mn ratio, and increases from MFN-2 to MFN-4 with increasing Fe/Ni ratio. Activation of the Jahn–Teller active Mn^{3+}/Mn^{4+} redox is known to induce significant unit cell volume changes during cycling, which can lead to poor cyclability in such materials [9, 40]. The Fe 2p spectrum displays well-defined peaks at 710.7 and 724.2 eV, characteristic of Fe^{3+}[38, 39]. The Fe 2p spectrum for MFN-1 and MFN-2, which contain only 3 % Fe, exhibits broadened peaks (Fig. 4b). This broadening is attributed to the weak Fe signal due to its low concentration, which results in a poor signal-to-noise ratio . Similarly, the Ni 2p region exhibits peaks at 854.4 eV ($2p_{3/2}$) and 872.1 eV ($2p_{1/2}$), along with distinct shake-up satellites, indicative of Ni^{2+} oxidation state across all samples [38, 39].

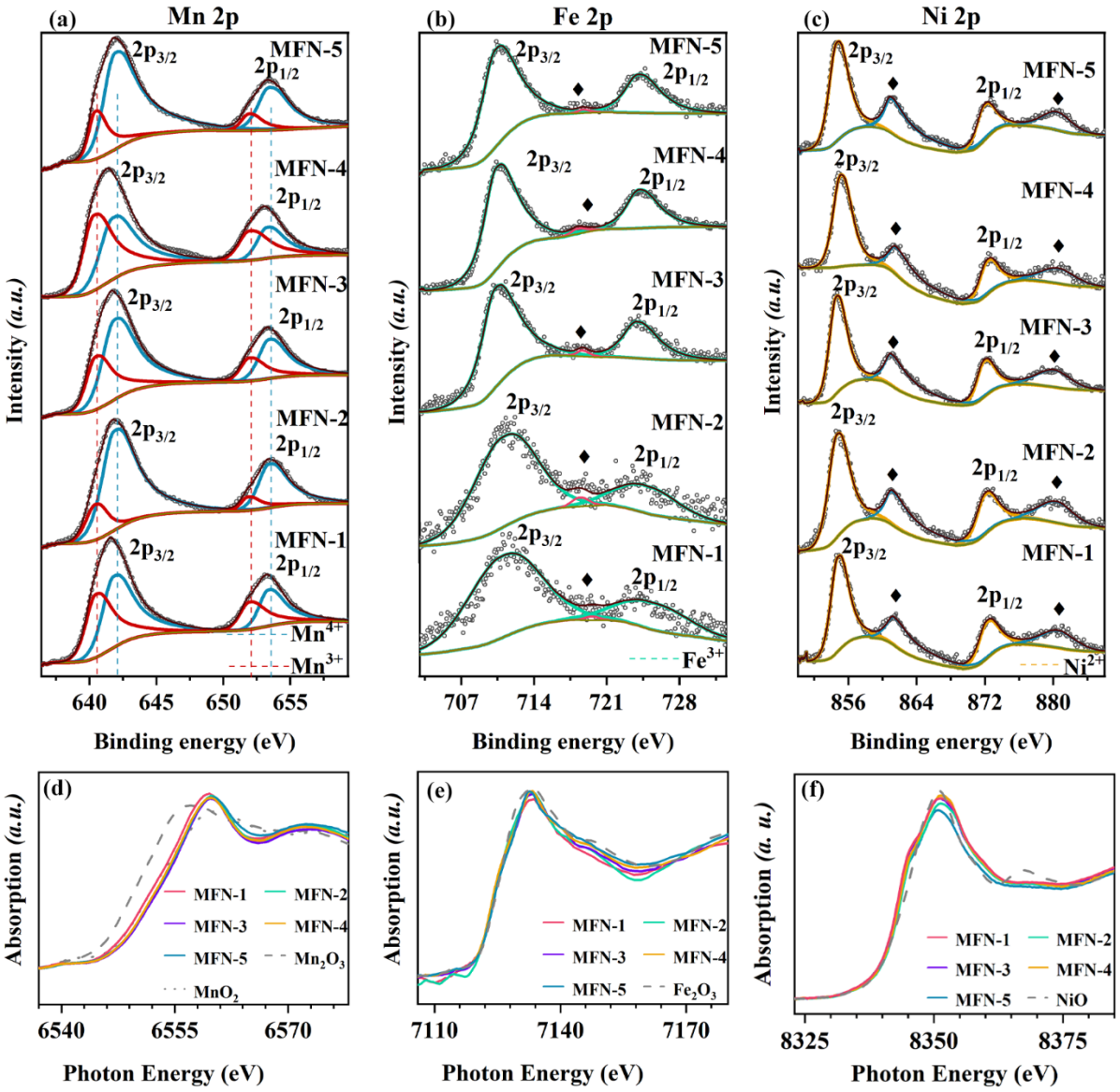

Fig. 4. (a) Mn 2p spectra, (b) Fe 2p spectra, and (c) Ni 2p spectra of the MFN samples calcined at 650 ℃ (♦ represents the shake-up satellite peaks in the Fe 2p and Ni 2p spectra). XANES spectra of MFN samples taken at (d) Mn K-edge, (e) Fe K-edge, and (f) Ni K-edge with relevant standard compounds.

To assess the bulk electronic environment, XAS measurements were carried out, and the Mn, Fe, and Ni K-edge X-ray absorption near edge structure (XANES) spectra are shown in Fig. 4 (d-f). The Mn K-edge positions lie between those of Mn_2O_3 and MnO_2 standards, confirming a mixed Mn^{3+}/Mn^{4+} valence state. The Ni K-edge profiles closely match that of NiO, affirming the presence of Ni^{2+}, while the Fe K-edge aligns with Fe_2O_3, consistent with the presence of Fe in the +3 state. These XANES results are consistent with the surface-sensitive XPS analysis.

3.2. Electrochemical properties

The electrochemical performance of the MFN samples was evaluated in the voltage ranges of 2.0 – 4.0 V and 2.0 – 4.4 V, with the corresponding galvanostatic charge-discharge (GCD) and differential capacity (dQ/dV vs. V) profiles at 0.1C presented in Fig. 5. These two voltage windows were selected to investigate the influence of varying Fe/Ni and Fe/Mn ratios on the high-voltage redox processes associated with Ni and Fe.

In the 2.0 – 4.0 V range, the specific discharge capacities of MFN-1, MFN-2, MFN-3, MFN-4, and MFN-5 are ~ 102, 94, 103, 88, and 108 mAh g^{-1}, respectively. When cycled in the broader 2.0 – 4.4 V range, the corresponding capacities increase to 109, 150, 134, 114, and 153 mAh g^{-1}.

At lower Fe/Mn and Fe/Ni ratios, the GCD curves exhibit more pronounced plateau features, whereas a higher Fe content results in more sloped profiles, indicative of a solid-solution-type reaction. This trend is also reflected in the dQ/dV curves, where sharper and well-defined redox peaks for compositions with lower Fe/Mn and Fe/Ni ratios become increasingly broadened and merged as Fe content rises. This suggests the suppression of Na^{+}/vacancy ordering during sodiation/desodiation with increasing Fe concentration.

Across all samples cycled in the 2.0 – 4.0 V range, redox peaks at ~ 3.19/3.15 V, 3.30/3.25 V, and 3.63/3.59 V are observed, corresponding to the $Ni^{2+/3+/4+}$ redox reaction [17, 18, 41]. Notably, MFN-1 and MFN-2 have an additional oxidation peak at 3.7 V and a plateau in the GCD curve without any corresponding reduction peak. This behavior is likely due to structural changes that may involve oxygen redox processes rather than further Ni redox activity, consistent with observations in other anionic redox-active materials [19, 42]. The capacity contribution from this is ~ 37 mAh g^{-1} for MFN-1 and ~ 34 mAh g^{-1} for MFN-2. The onset potential for these changes systematically shifts to higher voltages with increasing Fe/Mn and Fe/Ni ratios.

The initial coulombic efficiency (ICE) improves from 77.7% for MFN-2 to 98.5% for MFN-3 with increasing Fe/Ni ratios in the 2.0–4.0 V range. However, when cycled in the broader voltage range of 2.0 – 4.4 V, the ICE decreases for all samples. For instance, it drops from 98.5% to 89.8% for MFN-3 and from 95.3% to 79.3% for MFN-1, primarily due to partially irreversible redox reactions occurring above 4.0 V, as evidenced by the GCD and dQ/dV profiles shown in Fig. 5 (c) and (d) [24]. Above 4.0 V, the dQ/dV profiles reveal two distinct oxidation peaks, 4.02 and 4.23 V in MFN-1; 4.09 and 4.23 V in MFN-2; 4.03 and 4.23 V in MFN-3; 4.16 and 4.23 V in MFN-4; and 4.14 and 4.23 V in MFN-5. While the peak at ~ 4.23

V is common to all compositions and associated with high-voltage redox activity, the lower-voltage peaks (~ 4.02 – 4.16 V) vary with composition and are most prominent in MFN-1 and MFN-2. Given the low Fe content (~ 3%) in these two samples, the pronounced oxidation features at ~ 4.02 and 4.09 V cannot be solely attributed to Fe redox [19, 43]. Instead, these peaks can be assigned to several processes, such as a phase transition from P to O type, [44, 45] the formation of new phases (OP4 and/or Z phase) [26, 46, 47], or contributions from anionic redox of lattice oxygen, likely involving oxygen oxidation and possible O_2 evolution ($O^{2-}/O^{2n-}/O_2$). This is further supported by the presence of a flat charge plateau at high voltage and a sloping, less pronounced plateau during discharge (a typical feature of irreversible anionic redox) [48]. For MFN-1 and MFN-2, the high-voltage redox processes contribute capacities of ~ 46 and 84 mAh g^{-1}, respectively, during the first charging. The corresponding discharge capacities from these plateaus are significantly lower, contributing only ~ 8 and 20 mAh g^{-1} for MFN-1 and MFN-2, respectively.

In MFN-3, the initial charge process exhibits two distinct high-voltage oxidation peaks at 4.03 and 4.23 V. During discharge, however, the two expected reduction peaks merge into a single broad feature. In subsequent cycles, the first oxidation peak, originally observed at 4.03 V, shifts to a higher potential around 4.15 V, and both oxidation peaks coalesce into a broad peak centered at ~ 4.19 V. The corresponding reduction process also manifests as a broad peak near 3.99 V, indicating a less reversible and more diffuse redox process compared to the first cycle. MFN-5 displays two well-resolved reduction peaks at 4.04 and 3.95 V in the first cycle. Upon further cycling, the first oxidation peak shifts slightly to ~ 4.16 V but remains distinguishable, appearing as a shoulder before the second oxidation peak. The reduction peaks also remain separate, observed at 4.01 and 3.92 V in subsequent cycles. During charging, the high-voltage redox processes contribute 39 mAh g^{-1} for MFN-3 and 49 mAh g^{-1} for MFN-5, while discharge capacities are 23 mAh g^{-1} and 32 mAh g^{-1}, respectively. This behavior suggests a more reversible and stabilized redox process in MFN-5 compared to MFN-3. *Ex situ* XPS analysis was conducted to correlate these voltage-dependent redox features with Fe redox activity (Fig. S5 (Supplementary Material)). In MFN-3, the Fe redox contribution is negligible in the 2.0 – 4.0 V range and increases to ~ 0.07 Fe (~ 17.7 mAh g^{-1}) in the 2.0 – 4.4 V range. In contrast, MFN-5 exhibits a Fe redox activity of ~ 0.07 Fe (~ 17.7 mAh g^{-1}) in the 2.0 – 4.0 V and ~ 0.16 Fe (~ 40.3 mAh g^{-1}) in the 2.0 – 4.4 V range. These observations collectively indicate that increasing Fe content contributes to the stabilization of anionic redox activity. This stabilization may arise from competitive interactions between Fe and O redox processes. In Fe-containing

layered oxides, it has been reported that the charge compensation sequence during charging is altered, with Fe^{4+} reduction occurring first, followed by redox activity from oxygen and Ni at higher sodium contents [19, 20].

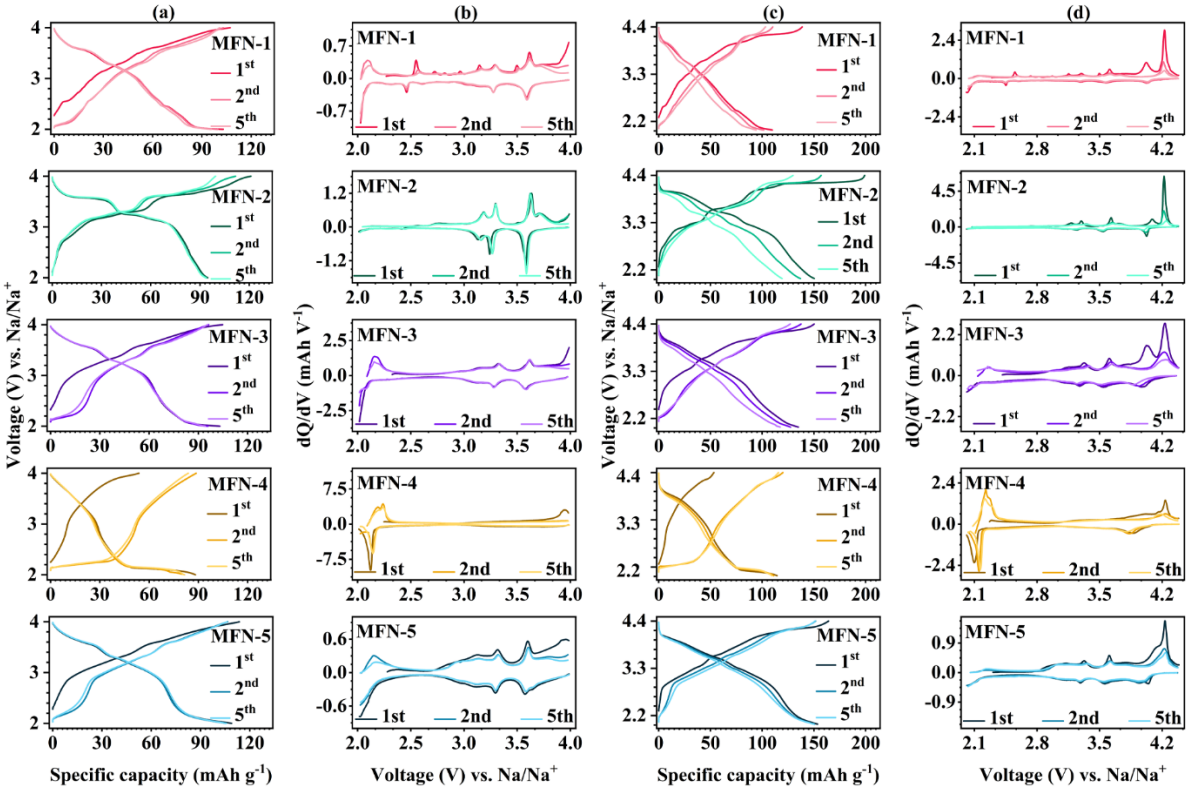

Fig. 5. (a,c) GCD curves and (b,d) dQ/dV profiles of the 1st, 2nd, and 5th cycles for MFN samples in the 2.0 – 4.0 V and 2.0 – 4.4 V ranges.

Another notable observation concerns the activation of Mn redox under different voltage windows. When cycled within the 2.0 – 4.0 V range, Mn^{4+} is reduced to Mn^{3+} after the initial charge, leading to the activation of the Mn redox couple in subsequent cycles. The activation of Mn is not desirable for long-term cycling, where the involvement of Jahn-Teller active Mn^{3+} ions is detrimental for cyclability [9, 40]. Cycling within the broader 2.0 – 4.4 V range significantly suppresses Mn redox activity. This is evident from the diminished Mn-related plateaus in the GCD curves and the weak corresponding features in the dQ/dV profiles. Interestingly, MFN-4, with the highest Fe/Ni ratio, exhibits a distinct behavior. Regardless of the voltage window, Mn^{4+} is reduced to Mn^{3+} during the first discharge, leading to Mn redox activation in the following cycles. The capacity obtained from Mn^{4+} reduction is ~ 40 mAh g^{-1} and corresponds to ~ 0.15 extra Na insertion in the material. Decreasing Ni content shifts the redox voltage for Mn activation to higher values. Additionally, MFN-4 displays only a subtle oxidation peak at ~ 4.16 V and a merged reduction peak at ~ 3.9 V. These results suggest that

the activation of Mn redox may suppress high-voltage redox activity, potentially due to the preferential involvement of Mn in the redox compensation mechanism [25].

The average potential is a key parameter influencing the overall energy density of the cathode material. For layered oxide cathodes, the average discharge voltage generally ranges from 2.3 to 3.4 V. Cathodes containing high-voltage redox-active transition metals, such as Ni and Fe, tend to exhibit higher average voltages [49]. The average voltage values and the corresponding specific energies (at the cathode level) of the MFN samples are given in Table 2. The lower average voltage of MFN-4 is attributed to the activation of the Mn^{4+}/Mn^{3+} redox couple, which occurs during the first discharge and contributes to sustained capacity in subsequent cycles. This redox activity takes place at lower potentials and dominates over high-voltage processes, effectively lowering the average voltage. The values of specific energies are higher in the wider voltage range due to the higher specific capacities and the elevated average voltages in the 2.0 – 4.4 V range. The highest specific energy approaches ~ 500 Wh kg^{-1} for MFN-5.

Table 2. A comparison of the electrochemical performance of MFN samples.

Sample	***ICE (%)***	***Average voltage (V)***	***Specific energy (Wh kg^{-1})***	***Capacity retention at 0.2C (of the capacity at 0.1C) (%)***	***Capacity retention at 1C (of the capacity at 0.1C) (%)***	***Capacity retention (%) after 100 cycles***
2.0 – 4.0 V						
MFN-1	95.3	3.02	308.0	83.00	28.32	76.47
MFN-2	77.7	3.26	306.0	84.95	38.71	77.50
MFN-3	98.5	3.17	326.5	90.90	62.56	99.0
MFN-4	166.0	2.28	200.6	89.28	53.57	62.16
MFN-5	95.6	3.10	334.8	88.23	62.75	88.89
2.0 – 4.4 V						
MFN-1	79.3	3.02	329.2	68.62	21.16	52.17

MFN-2	75.4	3.28	492.0	75.18	6.98	58.31
MFN-3	89.8	3.19	427.5	90.40	44.72	88.69
MFN-4	215.1	2.64	300.9	79.09	30.00	63.21
MFN-5	91.8	3.27	500.3	90.00	41.33	92.59

The rate capability of MFN cathodes was systematically investigated at varying C-rates within the 2.0 – 4.0 V and 2.0 – 4.4 V windows. The specific capacities obtained at different C-rates are presented in Fig. 6 (a, b), with corresponding capacity retentions summarized in Table 2. A progressive decrease in discharge capacity is observed with increasing C-rate for all compositions. Notably, upon returning to lower rates, the initial discharge capacities are recovered, indicating that the capacity losses are predominantly reversible. As expected, the broader voltage window (2.0 – 4.4 V) yields higher specific capacities. Among the compositions, MFN-3 and MFN-5, with elevated Fe/Mn ratios, demonstrate superior rate performance, retaining ~ 62% of the specific capacity at 1C compared to the capacity at 0.1C.

The superior rate performance of MFN-3 and MFN-5 correlates strongly with structural characteristics, where enhanced Na^+ diffusion kinetics are associated with wider Na-O_2 layer spacings resulting from increased Fe/Mn content. Additionally, SEM images reveal that MFN-3 and MFN-5 consist of well-defined particles with reduced agglomeration, which likely contributes to more efficient electrolyte wetting and shorter diffusion pathways. Although MFN-4 exhibits expanded Na-O_2 layer spacing, its rate performance is notably poor. This is attributed to its distinct morphology, characterized by thin, hexagonal plate-like particles with high aspect ratios. Such morphology can impede Na^+ transport, offsetting the potential advantages of increased interlayer distance.

The effect of varying Fe/Mn and Fe/Ni ratios on the cyclic stability of MFN cathodes was evaluated in the 2.0 – 4.0 V and 2.0 – 4.4 V windows. Fig. 6 (c, d) shows the specific capacities measured at 0.2C, while Fig. S6 (Supplementary Material) provides the GCD profiles for the 1^{st}, 5^{th}, 50^{th}, and 100^{th} cycles. Table 2 summarizes the corresponding capacity retentions after 100 cycles. In the 2.0 – 4.0 V range, the capacity retention ranges from ~ 76% to ~ 99%. Along the constant Ni line, increasing the Fe/Mn ratio initially improves capacity retention from 76.47% in MFN-1 to 99% in MFN-3, before slightly decreasing to ~ 88.9% in MFN-5. Along

the constant Mn line, a similar trend is observed where the capacity retention first improves from MFN-2 to MFN-3, but drops sharply to ~ 62.6% for MFN-4. This decline is attributed to the activation of Jahn–Teller active Mn^{3+} ions, as evidenced by the GCD results showing Mn^{4+} reduction in MFN-4 after the initial charge. This reduction triggers Mn redox in subsequent cycles, a process known to cause structural distortion and capacity fading.

When cycled in the broader 2.0 – 4.4 V window, the MFN samples exhibit varied cyclic stabilities. The cyclic performance curves for MFN-1 and MFN-2 show a rapid decay in specific capacity after only a few cycles of steady performance, consistent with rapid structural degradation due to the high voltage redox reactions and potential anionic redox in these cathodes with cycling. MFN-3, which showed nearly full retention when cycled in the 2.0 – 4.0 V range, maintains 88.69% retention in the broader voltage range. This is attributed to the structural transformations occurring at higher voltages, which will be discussed later.

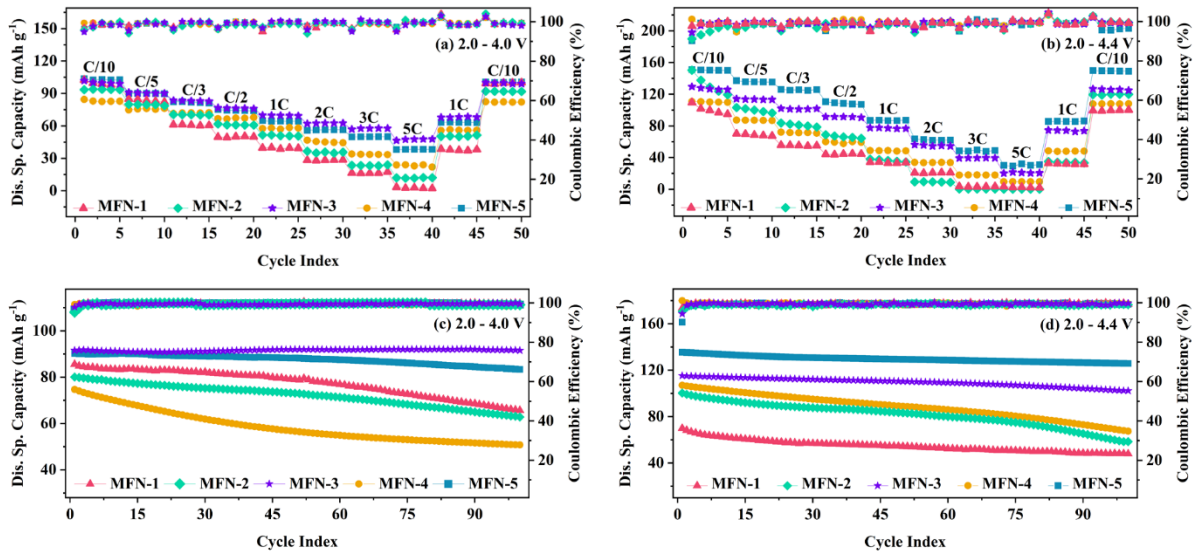

Fig. 6. Rate performance of MFN samples in (a) 2.0 – 4.0 V and (b) 2.0 – 4.4 V. Cyclability of MFN samples in (c) 2.0 – 4.0 V and (d) 2.0 – 4.4 V ranges.

Notably, MFN-5 shows improved cycling performance in the wider voltage range, retaining 92.6% of its capacity, higher than in the 2.0 – 4.0 V range. This result aligns with GCD and dQ/dV profiles, which reflect minimal voltage hysteresis and sustained electrochemical activity upon cycling. The enhanced long-term stability of MFN-5 is likely driven by its reversible and well-stabilized high-voltage redox processes. These findings are further supported by *operando* Synchrotron XRD (discussed later), which confirms structural stability during cycling.

Interestingly, the capacity retention of MFN-4 in the wider voltage window is similar to that in the 2.0 – 4.0 V. Previous reports suggest that the activation of the Mn^{3+}/Mn^{4+} redox couple at lower voltages is less detrimental to capacity retention than the high-voltage activation of Ni and anionic redox processes [25]. In this case, the similar retention across both voltage windows may arise from the suppression of high-voltage redox by activated Mn redox, as supported by the GCD results. Additionally, Fe redox may contribute to stabilizing Ni and anionic redox processes at high voltages, consistent with earlier studies [19, 41].

The Na-ion diffusion coefficient (D_{Na^+}) for the MFN cathodes was determined using the galvanostatic intermittent titration technique (GITT) in the 2.0 – 4.0 and 2.0 – 4.4 V ranges (Fig. S7). Prior to measurement, the cells underwent a formation cycle. During the GITT procedure, a constant current pulse at 0.1C was applied for 10 minutes, followed by a 30-minute rest period to allow the system to reach a near-equilibrium state. The diffusion behavior was analyzed based on Fick's first law, and D_{Na^+} values were calculated using the equation 5. [50]

$$D_{Na^+} = \frac{4}{\pi\tau}\left(\frac{m_B V_m}{M_B S}\right)^2 \left(\frac{\Delta E_S}{\Delta E_\tau}\right)^2 \qquad (t \ll L^2 / D) \qquad \ldots\ldots\ldots\ldots\ldots(5)$$

where:

τ is the duration of the constant current pulse,

m_B is the active material loading on the cathode,

V_m is the molar volume of the material,

M_B is the molecular weight of the material,

S is the surface area of the cathode,

$\Delta E\tau$ is the voltage change during the current pulse,

ΔE_S is the voltage change when the material reaches equilibrium.

The calculated D_{Na^+} values for all samples in 2.0 – 4.0 V and the 2.0 – 4.4 V ranges are given in Table S9 (Supplementary Material). In the 2.0 – 4.0 V range, MFN-3 exhibits the highest diffusion coefficients, ranging from 3.59×10^{-10} to 2.97×10^{-9} $cm^2\ s^{-1}$, consistent with its outstanding rate capability and cycling stability. Upon extending the voltage window to 4.4 V, a general decrease in diffusion coefficients is observed across all samples due to the slower

kinetics in this region. Notably, MFN-5 maintains relatively high diffusion coefficients (2.46×10^{-11} to 1.19×10^{-9} cm^2 s^{-1}) even in the wider voltage range, aligning with its superior high-voltage cyclability. In contrast, MFN-2 exhibits severely reduced diffusion kinetics (5.16×10^{-13} to 1.88×10^{-10} cm^2 s^{-1}), consistent with its poor structural stability and rapid capacity fade during cycling.

3.3. *Operando* Synchrotron XRD

The enhanced structural stability of MFN-5 and the detrimental influence of high-voltage redox activity on layered oxide structure were elucidated through *operando* Synchrotron XRD. The Synchrotron XRD patterns were recorded for MFN-2, MFN-3, and MFN-5 cells while cycling at a charge/discharge rate of 0.2 C between 2.0 and 4.4 V. Synchrotron XRD profiles for MFN-5 are shown in Fig. 7, with corresponding data for MFN-2 and MFN-3 presented in Figs. S6-S7 (Supplementary Material). These cathodes undergo a range of phase transitions, which vary across compositions depending on their transition metal ratios and initial phase fractions.

MFN-5, which exhibits a biphasic P2/O3 structure in the pristine state, displays sequential transformations in both phases at different states of charge and discharge. During charging, the (003) and (006) reflections of the O3 phase shift to higher angles, indicating increased electrostatic repulsion between oxygen layers upon Na^+ extraction, a characteristic feature of layered oxides. The O3 phase subsequently transforms into a monoclinic O3′ phase, as confirmed by the splitting of the $(104)_{hex}$ peak of the O3 phase into $(20\bar{2})_{mon}$ and $(111)_{mon}$ reflections of the O3′ phase (Fig. S8 (Supplementary Material)) [51]. This intermediate O3′ phase further evolves into a P3 phase. Concurrently, the P3 phase begins transforming into a P3′ phase, evidenced by the splitting of the $(105)_{hex}$ peak of the P3 phase into $(201)_{mon}$ and $(11\bar{2})_{mon}$ peaks in the P3' phase, and a decrease in the (104)/(015) intensity ratio to < 1 (Fig. S8 (Supplementary Material)).[31, 51] This P3 → P3′ transition is also observed in the monophasic P3 systems MFN-2 and MFN-3 at voltages < 4 V. Such transformations (O3 → O3′ → P3 and P3 → P3′), and their reversibility, have been widely reported for O3 and P3-type sodium layered oxides [6, 52, 53].

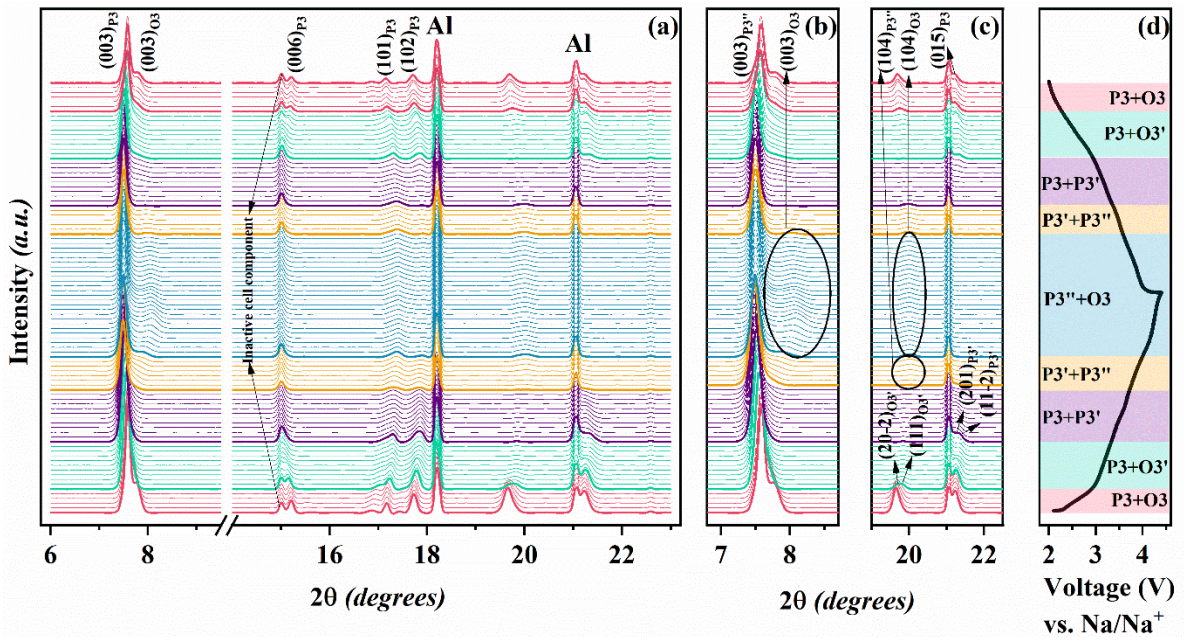

Fig. 7. (a) *Operando* Synchrotron XRD of MFN-5. Magnified view of (b) (003)P3 & (003)O3, (c) (104)O3 & (015)P3 peaks of MFN-5 showing various phase transformations in the material. (d) The corresponding GCD curve.

Accordingly, the focus of this study is on the phase transformations occurring above 4 V and their implications on the electrochemical properties of the materials. In MFN-2, an increase in (104) peak intensity (I_{104}) and the simultaneous decrease in I_{015} results in a (104)/(015) ratio > 1, indicating the re-emergence of the O3 phase [45, 54, 55]. A complete transformation to the O3 phase is observed above 4.2 V (Fig. S9 (b)). Upon discharge, the material reverts to the P3 phase via a P3′ intermediate, suggesting a reversible P3 ↔ P3′ ↔ O3 transformation. MFN-3 displays a high-voltage transition to a P3″ phase beyond 4.1 V, characterized by broadening of the (003) peak as indicated in Fig. S10 (b) [51]. The P3″ phase subsequently reverts to the P3 phase through P3′ during discharge, indicative of a reversible P3 ↔ P3′ ↔ P3″ transformation. In MFN-5, both O3 and P3″ phases are present at high voltage, as evidenced by the emergence of the (104)O3 reflection. Concomitantly, the (003) peak also shifts to higher angles, indicating a reduction in the *c* parameter (Fig. 7 (a)). Upon discharge, MFN-5 undergoes a reversible transformation back to the original biphasic P3/O3 structure.

Quantitative analysis of the variations in the lattice parameters of MFN cathodes was performed via Le Bail refinement of *operando* Synchrotron XRD data at different states of charge and discharge. The variations of the lattice parameters during charging/discharging are presented in Tables S10-S12 (Supplementary Material). The change in the c parameter (Δc =

$\frac{c_{4.4V}-c_{2.0V}}{c_{4.4V}} \times 100\%$) of the is ~ 1.47% for MFN-2, ~1.18% for MFN-3 (both in the P3 phase), and −1.81% (O3) and +1.00% (P3) for MFN-5 during discharge from 4.4 V to 2.0 V.

3.4. Discussion

The electrochemical, structural, and redox analyses collectively reveal the critical role of phase evolution and compositional tuning in dictating the cycling stability of the MFN cathodes. *Operando* Synchrotron XRD demonstrates a clear P3 → P3′ phase transition for MFN-2 and MFN-3 within the 2.0 – 4.0 V range. In the P3′ phase, all Na ions occupy one prismatic site, which is surrounded by TM-O_6 octahedra sharing a face on one side and edges on the other [56]. The relatively modest in-plane distortion associated with the P3′ structure, compared to the monoclinic distortions in O3′ and P3″ phases, confers MFN-3 with superior structural stability [51]. This stabilization accounts for the remarkable cycling performance of MFN-3 in the 2.0 – 4.0 V range, outperforming all other samples. Although MFN-2 also undergoes a P3 → P3′ transition, its minimal Fe content triggers additional redox activity at potentials below 4.0 V, as evidenced by GCD and dQ/dV analyses. This leads to structural destabilization, contributing to the inferior cyclability of MFN-2 relative to MFN-3.

Beyond 4.0 V, MFN-3 undergoes a transformation from the stable P3′ phase to a less stable P3″ phase, which induces lattice strain, contributing to structural instability. MFN-5, in contrast, demonstrates outstanding cycling stability over an extended 2.0 – 4.4 V window, attributed to the synergistic interplay between its biphasic P3/O3 structure and Fe-mediated redox stabilization. The coexisting phases induce the *interlocking effect*, which buffers the internal strain generated during cycling and prevents excessive strain accumulation and lattice collapse. Simultaneously, the increased Fe content in MFN-5 appears to contribute significantly to chemical stabilization. Fe^{4+} formation during charge effectively competes with the oxygen redox, delaying or even suppressing irreversible oxygen loss that often triggers structural degradation. During discharge, Fe redox precedes the O-redox and ensures that any oxygen redox activity occurs in a more controlled and reversible manner [19, 57, 58]. These findings are further supported by *ex situ* XPS analysis, which confirms greater Fe redox participation in MFN-5, particularly above 4.0 V. This earlier onset of Fe^{4+} formation in MFN-5 supports a redox sequence that stabilizes high-voltage processes by reducing anionic redox. In contrast, MFN-3 shows a higher oxygen participation at elevated voltages, which contributes to lattice strain and poorer reversibility. The enhanced Fe activity in MFN-5 promotes a redox environment that suppresses anionic redox activity and supports structural stability,

complementing the strain-buffering effect of the biphasic P3/O3 framework. Thus, MFN-5 benefits from a dual-stabilization mechanism: lattice strain mitigation via structural interlocking and chemical stabilization through Fe redox. This synergistic approach enhances the structural integrity of the cathode and significantly improves its high voltage cycling performance.

3.5. Full cell

Full cells were assembled using MFN-5 as the cathode and hard carbon as the anode material. Before integration, the hard carbon anode was cycled twice in a half-cell configuration with sodium metal as the counter electrode. The cycled hard carbon was then recovered by decrimping the cell and employed in the full-cell assembly. The anode-to-cathode capacity ratio (N/P ratio) was optimized to 0.9, based on prior studies and the half-cell performance of both electrodes [59]. The hard carbon anode delivered a specific capacity of ~ 259 mAh g^{-1} in the second cycle Fig. 8(a)).

The full cell was cycled at 0.1C in a voltage window of 1.0 to 4.0 V, achieving a specific capacity of ~ 86 mAh g^{-1} (based on the active mass of the cathode) with an average discharge voltage of ~ 3.2 V (Fig. 8 (b)). The system exhibited a notable rate capability, retaining ~ 75% discharge capacity at 0.5C of the capacity at 0.1C (Fig. 8(c)). At 0.2C, the full cell delivered an initial discharge capacity of 77.4 mAh g^{-1}, with 64.6 mAh g^{-1} remaining after 100 cycles, corresponding to 83.1% capacity retention (Fig. 8(d)). To further investigate the high-voltage behavior of MFN-5 in a full-cell configuration, additional tests were conducted in the 1.0 – 4.2 V range (Fig. S11, Supplementary Material). The cell delivered a specific capacity of ~94.1 mAh g^{-1} with 79.7% capacity retention after 50 cycles. These results demonstrate that MFN-5 based full cells, with a high operating voltage and stable cyclic performance, are promising for practical Na-ion battery applications.

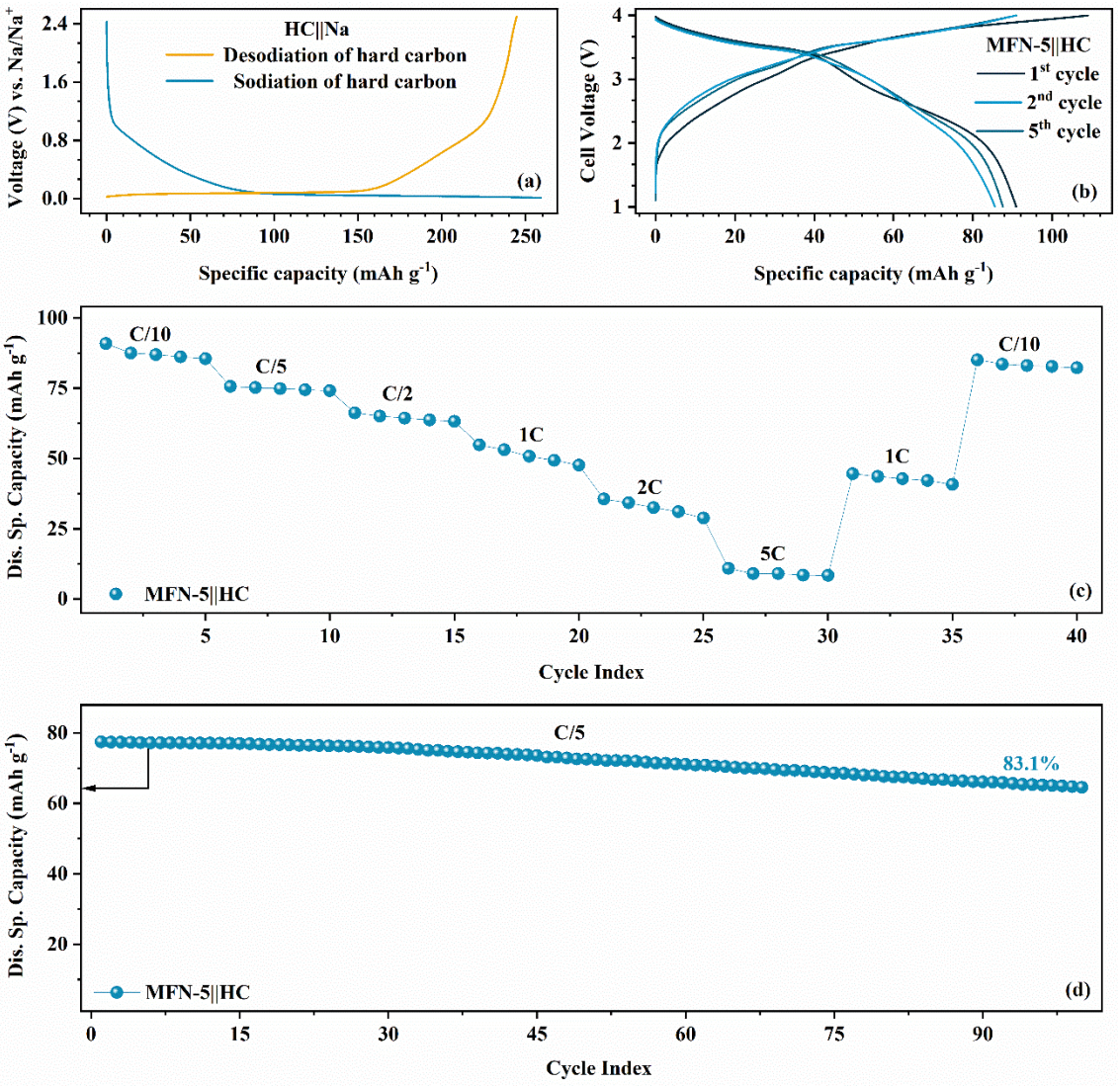

Fig. 8. (a) Charge-discharge curve of hard carbon versus Na metal, (b) The 1st, 2nd, and 5th cycle GCD curves of full cell with MFN-5 cathode and HC anode at 0.1C, (c) Rate performance of MFN-5||HC full cell at various C-rates, and (d) Cyclic performance of MFN-5||HC full cell at 0.2C for 100 cycles.

4. CONCLUSIONS

This work presents a detailed investigation into the structural and electrochemical behavior of various compositions in $Na_{0.8}(Mn–Fe–Ni)O_2$ system with varying Fe/Mn and Fe/Ni ratios in the 2.0 – 4.0 V and 2.0 – 4.4 V ranges. Structural analysis confirms a dominant P3-type layered structure in all samples, with MFN-5 having the highest Fe/Mn ratio, exhibiting a biphasic P3/O3 configuration (~ 24% O3). Rietveld refinement shows a systematic expansion of the *c* parameter and Na layer spacing with increasing Fe/Mn and Fe/Ni ratio, while EXAFS at the Mn K-edge indicates Mn–O bond shortening, indicating stronger TM–O interactions. FESEM

images reveal spheroidal particles, with increasing Fe/Ni ratio leading to larger average particle sizes, and MFN-4 uniquely displaying coexisting plate-like particles. HRTEM and SAED further confirm well-ordered P3-type frameworks and reveal distinct superlattice configurations $(2\sqrt{3} \times 2\sqrt{3})$-R30° and $(\sqrt{3} \times \sqrt{3})$-R30°) dependent on Fe content, highlighting the influence of transition metal composition on local ordering.

All MFN samples exhibited increased specific capacity in the 2.0 – 4.4 V range. MFN-5 achieved the highest capacity of 153 mAh g^{-1} in the 2.0 – 4.4 V range, yielding a cathode-level specific energy of ~ 500 Wh kg^{-1} and an average voltage of 3.27 V. Importantly, MFN-5 also exhibits superior long-term cyclability in this extended range, retaining 92.6% capacity after 100 cycles. This is attributed to a favorable redox sequence in which more $Fe^{3+/4+}$ activate prior to oxygen during charging, delaying anionic redox and structural degradation. MFN-3 stands out as the most stable composition in the narrower 2.0 – 4.0 V range, retaining 99% capacity over 100 cycles at 0.2C, the best among all samples. This exceptional stability is linked to a reversible P3 → P3′ transition and the suppression of oxygen redox below 4.0 V, enabling highly reversible Ni and Fe redox without structural degradation.

Operando Synchrotron XRD studies provide a structural basis for these electrochemical trends. MFN-5 exhibits reversible phase transitions with minimal lattice strain ($\Delta c = -1.81\%$ for O3 and +1.00% for P3), enabled by the phase interlocking between the P3 and O3 phases. This structural synergy stabilizes the cathode during extended cycling and correlates directly with preserved redox features and minimal voltage hysteresis. Full-cell testing with MFN-5 as the cathode and hard carbon anode validates its practical potential, achieving 86 mAh g^{-1} at 0.1C, a median discharge voltage of 3.2 V, and 83.1% retention over 100 cycles at 0.2C. In summary, this study demonstrates that careful tuning of Fe/Mn and Fe/Ni ratios enables control over redox behavior and structural transformations in MFN cathodes. MFN-5, with its superior high-voltage redox performance and dual stabilization mechanisms, namely Fe-mediated redox buffering and P3/O3 phase interlocking, provides a way forward for designing durable, energy-dense sodium-ion batteries.

CRediT authorship contribution statement

Samriddhi Saxena: Conceptualization, Data curation, Formal analysis, Investigation, Methodology, Validation, Writing – original draft. **Neha Dagar:** Writing – review & editing. **Velaga Srihari:** Data curation, Writing – review & editing. **Karthik Chinnathambi:** Data curation, Writing – review & editing. **Asish Kumar Das:** Writing – review & editing.

Pratiksha Gami: Writing – review & editing. **Sonia Deswal:** Writing – review & editing. **Pradeep Kumar:** Data curation, Writing – review & editing. **Himanshu Kumar Poswal:** Writing – review & editing. **Sunil Kumar:** Funding acquisition, Project administration, Supervision, Validation, Writing – review & editing.

Declaration of competing interest

The authors declare that they have no known competing financial interests or personal relationships that could have appeared to influence the work reported in this paper.

Acknowledgments

This work was financially supported by the Ministry of Education (grant number: MoE-STARS/STARS-2/2023-0365), Government of India. SS thanks the Ministry of Education, Government of India, for the Prime Minister's Research Fellowship (grant number: 2103359). This research utilized the Transmission Electron Microscope (TEM) in the Boise State University FaCT Core Facility, RRID: SCR_024733, which receives support from the National Institutes of Health [NIH] under the Institutional Development Awards [IDeA] Program of the National Institute of General Medical Sciences [NIGMS] via grants P20GM148321 and P20GM103408. The authors acknowledge the Sophisticated Instrumentation Centre (SIC), IIT Indore, for providing the ICP-OES analytical facility and Dr. Biplab Ghosh for his help in recording the EXAFS spectra at RRCAT, Indore, India.

Data availability

Data will be made available on request.

REFERENCES

1. Yong-Mook Kang, Anmin Cao, Raphaële Clément, Shu-Lei Chou, Sang-Young Lee, Zongcheng Miao, *"Battery technology and sustainable energy storage and conversion as a new energy resource replacing fossil fuels"*, **Battery Energy** 1(1) (2022) 20220200. https://doi.org/10.1002/bte2.20220200.

2. Jang Wook Choi, Doron Aurbach, *"Promise and reality of post-lithium-ion batteries with high energy densities"*, **Nature Reviews Materials** 1(4) (2016) 16013. https://doi.org/10.1038/natrevmats.2016.13.

3. Eider Goikolea, Verónica Palomares, Shijian Wang, Idoia Ruiz de Larramendi, Xin Guo, Guoxiu Wang, Teofilo Rojo, *"Na-Ion Batteries—Approaching Old and New Challenges"*,

Advanced Energy Materials 10(44) (2020) 2002055. https://doi.org/10.1002/aenm.202002055.

4. Qiuyu Shen, Yongchang Liu, Lifang Jiao, Xuanhui Qu, Jun Chen, *"Current state-of-the-art characterization techniques for probing the layered oxide cathode materials of sodium-ion batteries"*, **Energy Storage Materials** 35 (2021) 400-430. https://doi.org/10.1016/j.ensm.2020.11.002.

5. Fatima Tasneem Mohsin, Nazmul Hossain, Tamzeed Ahmed Alvy, Tasnuva Sharmin, Md Azazul Haque, Mohammad Muhtasim Mashfy, Mohammed Mousa, Mohammad Nasim, *"Exploring the limitations and unlocking the potential of sodium-ion battery cathodes"*, **Materials Today Energy** 50 (2025) 101868. https://doi.org/10.1016/j.mtener.2025.101868.

6. Xiaoqin Chen, Chenkai Wang, Yu Zhao, Yongxin Wang, Xiaoju Yin, Naiqing Zhang, *"Recent progress in layered oxide cathodes for sodium-ion batteries: stability, phase transition and solutions"*, **Journal of Materials Chemistry A** 12(46) (2024) 31797-31817. https://doi.org/10.1039/D4TA03372H.

7. Hanqing Gao, Jinjue Zeng, Zhipeng Sun, Xiangfen Jiang, Xuebin Wang, *"Advances in layered transition metal oxide cathodes for sodium-ion batteries"*, **Materials Today Energy** 42 (2024) 101551. https://doi.org/10.1016/j.mtener.2024.101551.

8. C. Delmas, C. Fouassier, P. Hagenmuller, *"Structural classification and properties of the layered oxides"*, **Physica B+C** 99(1) (1980) 81-85. https://doi.org/10.1016/0378-4363(80)90214-4.

9. Kei Kubota, Takuya Asari, Shinichi Komaba, *"Impact of Ti and Zn Dual-Substitution in P2 Type $Na_{2/3}Ni_{1/3}Mn_{2/3}O_2$ on Ni–Mn and Na-Vacancy Ordering and Electrochemical Properties"*, **Advanced Materials** 35(26) (2023) 2300714. https://doi.org/10.1002/adma.202300714.

10. Hari Narayanan Vasavan, Samriddhi Saxena, Velaga Srihari, Asish Kumar Das, Pratiksha Gami, Neha Dagar, Sonia Deswal, Pradeep Kumar, Himanshu Kumar Poswal, Sunil Kumar, *"Elevating the Concentration of Na Ions to 1 in P2 Type Layered Oxide Cathodes"*, **Advanced Functional Materials** n/a(n/a) (2025) 2421733. https://doi.org/10.1002/adfm.202421733.

11. Qun Huang, Yiming Feng, Lei Wang, Shuo Qi, Pingge He, Xiaobo Ji, Chaoping Liang, Shuangqiang Chen, Liangjun Zhou, Weifeng Wei, *"Structure modulation strategy for suppressing high voltage P3-O1 phase transition of O3-$NaMn_{0.5}Ni_{0.5}O_2$ layered cathode"*,

Chemical Engineering Journal 431 (2022) 133454. https://doi.org/10.1016/j.cej.2021.133454.

12. Samriddhi Saxena, Manish Badole, Hari Narayanan Vasavan, Velaga Srihari, Asish Kumar Das, Pratiksha Gami, Neha Dagar, Sonia Deswal, Pradeep Kumar, Himanshu Kumar Poswal, Sunil Kumar, *"Elucidating the Electrochemical Behavior of a P3-type High-Na-Content Cathode"*, **Energy & Fuels** 38(13) (2024) 12140-12149. https://doi.org/10.1021/acs.energyfuels.4c01476.

13. Hari Narayanan Vasavan, Manish Badole, Samriddhi Saxena, Velaga Srihari, Asish Kumar Das, Pratiksha Gami, Sonia Deswal, Pradeep Kumar, Sunil Kumar, *"Unveiling the Potential of P3 Phase in Enhancing the Electrochemical Performance of a Layered Oxide Cathode"*, **Materials Today Energy** (2023) 101380. https://doi.org/10.1016/j.mtener.2023.101380.

14. Hari Narayanan Vasavan, Manish Badole, Samriddhi Saxena, Velaga Srihari, Asish Kumar Das, Pratiksha Gami, Neha Dagar, Sonia Deswal, Pradeep Kumar, Himanshu Kumar Poswal, Sunil Kumar, *"Identification of optimal composition with superior electrochemical properties along the zero Mn^{3+} line in $Na_{0.75}(Mn\text{-}Al\text{-}Ni)O_2$ pseudo ternary system"*, **Journal of Energy Chemistry** 96 (2024) 206-216. https://doi.org/10.1016/j.jechem.2024.04.015.

15. Dingan Cai, Yinda Li, Yunhao Lu, Bo Xu, Jicheng Jiang, Aijun Zhou, Xiongwen Xu, Jian Tu, Shengming Yu, Bin Pan, Xinbing Zhao, Jian Xie, *"Moisture-stable O3-type low-Ni layered oxides with improved electrochemical performance by Mg/Cu co-doping-enabled structural fine-tuning"*, **Materials Today Energy** 48 (2025) 101781. https://doi.org/10.1016/j.mtener.2024.101781.

16. Samriddhi Saxena, Hari Narayanan Vasavan, Neha Dagar, Karthik Chinnathambi, Velaga Srihari, Asish Kumar Das, Pratiksha Gami, Sonia Deswal, Pradeep Kumar, Himanshu Kumar Poswal, Sunil Kumar, *"Probing the Compositional and Structural Effects on the Electrochemical Performance of $Na(Mn\text{-}Fe\text{-}Ni)O_2$ Cathodes in Sodium-Ion Batteries"*, **Battery Energy** (2025) e70018. https://doi.org/10.1002/bte2.20240083.

17. Qiong Yang, Peng-Fei Wang, Jin-Zhi Guo, Zi-Ming Chen, Wei-Lin Pang, Ke-Cheng Huang, Yu-Guo Guo, Xing-Long Wu, Jing-Ping Zhang, *"Advanced P2-$Na_{2/3}Ni_{1/3}Mn_{7/12}Fe_{1/12}O_2$ Cathode Material with Suppressed P2–O2 Phase Transition toward High-Performance Sodium-Ion Battery"*, **ACS Applied Materials & Interfaces** 10(40) (2018) 34272-34282. https://doi.org/10.1021/acsami.8b12204.

18. J. W. Somerville, R. A. House, N. Tapia-Ruiz, A. Sobkowiak, S. Ramos, A. V. Chadwick, M. R. Roberts, U. Maitra, P. G. Bruce, *"Identification and characterisation of high energy density P2-type $Na_{2/3}[Ni_{1/3-y/2}Mn_{2/3-y/2}Fe_y]O_2$ compounds for Na-ion batteries"*, **Journal of Materials Chemistry A** 6(13) (2018) 5271-5275. https://doi.org/10.1039/C7TA09607K.

19. Edouard Boivin, Robert A. House, John-Joseph Marie, Peter G. Bruce, *"Controlling Iron Versus Oxygen Redox in the Layered Cathode $Na_{0.67}Fe_{0.5}Mn_{0.5}O_2$: Mitigating Voltage and Capacity Fade by Mg Substitution"*, **Advanced Energy Materials** 12(30) (2022) 2200702. https://doi.org/10.1002/aenm.202200702.

20. Gaurav Assat, Dominique Foix, Charles Delacourt, Antonella Iadecola, Rémi Dedryvère, Jean-Marie Tarascon, *"Fundamental interplay between anionic/cationic redox governing the kinetics and thermodynamics of lithium-rich cathodes"*, **Nature Communications** 8(1) (2017) 2219. https://doi.org/10.1038/s41467-017-02291-9.

21. Neha Dagar, Samriddhi Saxena, Hari Narayanan Vasavan, Asish Kumar Das, Pratiksha Gami, Sonia Deswal, Pradeep Kumar, Karthik Chinnathambi, Vikram Rathee, Sunil Kumar, *"Ti-Substitution Facilitating Anionic Redox and Cycle Stability in a P2-Type Na2/3Mn2/3Ni1/3O2 Na-Ion Battery Cathode"*, **Energy & Fuels** 39(6) (2025) 3348-3358. https://doi.org/10.1021/acs.energyfuels.4c05945.

22. C. Li, F. Geng, B. Hu, B. Hu, *"Anionic redox in Na-based layered oxide cathodes: a review with focus on mechanism studies"*, **Materials Today Energy** 17 (2020) 100474. https://doi.org/10.1016/j.mtener.2020.100474.

23. Yao Wang, Xudong Zhao, Junteng Jin, Qiuyu Shen, Yang Hu, Xiaobai Song, Han Li, Xuanhui Qu, Lifang Jiao, Yongchang Liu, *"Boosting the Reversibility and Kinetics of Anionic Redox Chemistry in Sodium-Ion Oxide Cathodes via Reductive Coupling Mechanism"*, **Journal of the American Chemical Society** 145(41) (2023) 22708-22719. https://doi.org/10.1021/jacs.3c08070.

24. Edouard Boivin, Robert A. House, Miguel A. Pérez-Osorio, John-Joseph Marie, Urmimala Maitra, Gregory J. Rees, Peter G. Bruce, *"Bulk O2 formation and Mg displacement explain O-redox in $Na_{0.67}Mn_{0.72}Mg_{0.28}O_2$"*, **Joule** 5(5) (2021) 1267-1280. https://doi.org/10.1016/j.joule.2021.04.006.

25. Liangtao Yang, Yanan Sun, Philipp Adelhelm, *"Electrochemical Properties of Layered $Na_xNi_{x/2}Mn_{1-x/2}O_2$ $(0.5 \leq x \leq 1.1)$ with P3 Structure as Cathode for Sodium-Ion Batteries"*, **Energy Technology** 10(4) (2022) 2101121. https://doi.org/10.1002/ente.202101121.

26. James W. Somerville, Adam Sobkowiak, Nuria Tapia-Ruiz, Juliette Billaud, Juan G. Lozano, Robert A. House, Leighanne C. Gallington, Tore Ericsson, Lennart Häggström, Matthew R. Roberts, Urmimala Maitra, Peter G. Bruce, *"Nature of the "Z"-phase in layered Na-ion battery cathodes"*, **Energy & Environmental Science** 12(7) (2019) 2223-2232. https://doi.org/10.1039/C8EE02991A.

27. Jang-Yeon Hwang, Seung-Taek Myung, Doron Aurbach, Yang-Kook Sun, *"Effect of nickel and iron on structural and electrochemical properties of O3 type layer cathode materials for sodium-ion batteries"*, **Journal of Power Sources** 324 (2016) 106-112. https://doi.org/10.1016/j.jpowsour.2016.05.064.

28. Yong Liang, Wanmin Liu, Hu Wu, Zexun Tang, Lv Xu, *"Developing high-performance sodium-ion battery cathode materials through regulating the Ni/Fe ratio in $Na_{0.67}Ni_xFe_{0.52-x}Mn_{0.48}O_2$"*, **Journal of Power Sources** 617 (2024) 235159. https://doi.org/10.1016/j.jpowsour.2024.235159.

29. Samriddhi Saxena, Hari Narayanan Vasavan, Neha Dagar, Velaga Srihari, Asish Kumar Das, Pratiksha Gami, Sonia Deswal, Pradeep Kumar, Himanshu Kumar Poswal, Sunil Kumar, *"Strategic phase modulation in $Na_{0.8}$(Mn-Fe-Ni)O_2 system delivers high energy density and structural stability"*, **Journal of Power Sources** 644 (2025) 237115. https://doi.org/10.1016/j.jpowsour.2025.237115.

30. Alan A. Coelho, *"TOPAS and TOPAS-Academic: an optimization program integrating computer algebra and crystallographic objects written in C++"*, **Journal of Applied Crystallography** 51(1) (2018) 210-218. https://doi.org/10.1107/S1600576718000183.

31. Shou-Hang Bo, Xin Li, Alexandra J. Toumar, Gerbrand Ceder, *"Layered-to-Rock-Salt Transformation in Desodiated Na_xCrO_2 (x 0.4)"*, **Chemistry of Materials** 28(5) (2016) 1419-1429. https://doi.org/10.1021/acs.chemmater.5b04626.

32. Shipeng Jia, Jonathan Counsell, Michel Adamič, Antranik Jonderian, Eric McCalla, *"High-throughput design of Na–Fe–Mn–O cathodes for Na-ion batteries"*, **Journal of Materials Chemistry A** 10(1) (2022) 251-265. https://doi.org/10.1039/D1TA07940A.

33. Samriddhi Saxena, Manish Badole, Hari Narayanan Vasavan, Velaga Srihari, Asish Kumar Das, Pratiksha Gami, Sonia Deswal, Pradeep Kumar, Sunil Kumar, *"Deciphering the role of optimal P2/O3 phase fraction in enhanced cyclability and specific capacity of layered oxide cathodes"*, **Chemical Engineering Journal** 485 (2024) 149921. https://doi.org/10.1016/j.cej.2024.149921.

34. Haoji Wang, Hongyi Chen, Yu Mei, Jinqiang Gao, Lianshan Ni, Ningyun Hong, Baichao Zhang, Fangjun Zhu, Jiangnan Huang, Kai Wang, Wentao Deng, Debbie S. Silvester, Craig E. Banks, Sedat Yasar, Bai Song, Guoqiang Zou, Hongshuai Hou, Xiaobo Ji, *"Manipulating Local Chemistry and Coherent Structures for High-Rate and Long-Life Sodium-Ion Battery Cathodes"*, **ACS Nano** 18(20) (2024) 13150-13163. https://doi.org/10.1021/acsnano.4c02017.

35. L. Wang, F. Zhou, Y. S. Meng, G. Ceder, *"First-principles study of surface properties of $LiFePO_4$: Surface energy, structure, Wulff shape, and surface redox potential"*, **Physical Review B** 76(16) (2007) 165435. https://doi.org/10.1103/PhysRevB.76.165435.

36. Robert A. House, Urmimala Maitra, Miguel A. Pérez-Osorio, Juan G. Lozano, Liyu Jin, James W. Somerville, Laurent C. Duda, Abhishek Nag, Andrew Walters, Ke-Jin Zhou, Matthew R. Roberts, Peter G. Bruce, *"Superstructure control of first-cycle voltage hysteresis in oxygen-redox cathodes"*, **Nature** 577(7791) (2020) 502-508. https://doi.org/10.1038/s41586-019-1854-3.

37. Yuansheng Shi, Pengfeng Jiang, Shicheng Wang, Weixin Chen, Bin Wei, Xueyi Lu, Guoyu Qian, Wang Hay Kan, Huaican Chen, Wen Yin, Yang Sun, Xia Lu, *"Slight compositional variation-induced structural disorder-to-order transition enables fast Na^+ storage in layered transition metal oxides"*, **Nature Communications** 13(1) (2022) 7888. https://doi.org/10.1038/s41467-022-35597-4.

38. Sheng Feng, Chujun Zheng, Zhiyang Song, Xiangwei Wu, Meifen Wu, Fangfang Xu, Zhaoyin Wen, *"Boosting fast ionic transport and stability of O3-$NaNi_{1/3}Fe_{1/3}Mn_{1/3}O_2$ cathode via Al/Cu synergistically modulating microstructure for high-rate sodium-ion batteries"*, **Chemical Engineering Journal** 475 (2023) 146090. https://doi.org/10.1016/j.cej.2023.146090.

39. Jill Chastain, Roger C King Jr, *"Handbook of X-ray photoelectron spectroscopy"*, **Perkin-Elmer Corporation** 40 (1992) 221.

40. Chen Cheng, Haolv Hu, Cheng Yuan, Xiao Xia, Jing Mao, Kehua Dai, Liang Zhang, *"Precisely modulating the structural stability and redox potential of sodium layered cathodes through the synergetic effect of co-doping strategy"*, **Energy Storage Materials** 52 (2022) 10-18. https://doi.org/10.1016/j.ensm.2022.07.030.

41. Vitalii A. Shevchenko, Iana S. Glazkova, Daniil A. Novichkov, Irina Skvortsova, Alexey V. Sobolev, Artem M. Abakumov, Igor A. Presniakov, Oleg A. Drozhzhin, Evgeny V. Antipov, *"Competition between the Ni and Fe Redox in the O3-$NaNi_{1/3}Fe_{1/3}Mn_{1/3}O_2$ Cathode Material*

for Na-Ion Batteries", **Chemistry of Materials** 35(10) (2023) 4015-4025. https://doi.org/10.1021/acs.chemmater.3c00338.

42. Jiaxin Yan, Yuanheng Wang, Qingjie Zhou, Xin Chen, Haixia Yang, Xingyu Wang, Jianting Li, Xing Xu, Zaifang Yuan, Pengjian Zuo, *"Improved anionic redox reversibility of layered oxides by modulating transition metal–oxygen bonds for sodium ion batteries"*, **Journal of Materials Chemistry A** (2025). https://doi.org/10.1039/D5TA00231A.

43. Urmimala Maitra, Robert A. House, James W. Somerville, Nuria Tapia-Ruiz, Juan G. Lozano, Niccoló Guerrini, Rong Hao, Kun Luo, Liyu Jin, Miguel A. Pérez-Osorio, Felix Massel, David M. Pickup, Silvia Ramos, Xingye Lu, Daniel E. McNally, Alan V. Chadwick, Feliciano Giustino, Thorsten Schmitt, Laurent C. Duda, Matthew R. Roberts, Peter G. Bruce, *"Oxygen redox chemistry without excess alkali-metal ions in $Na_{2/3}[Mg_{0.28}Mn_{0.72}]O_2$"*, **Nature Chemistry** 10(3) (2018) 288-295. https://doi.org/10.1038/nchem.2923.

44. Ya-Nan Zhou, Peng-Fei Wang, Xu-Dong Zhang, Lin-Bo Huang, Wen-Peng Wang, Ya-Xia Yin, Sailong Xu, Yu-Guo Guo, *"Air-Stable and High-Voltage Layered P3-Type Cathode for Sodium-Ion Full Battery"*, **ACS Applied Materials & Interfaces** 11(27) (2019) 24184-24191. https://doi.org/10.1021/acsami.9b07299.

45. Tim Risthaus, Lifang Chen, Jun Wang, Jinke Li, Dong Zhou, Li Zhang, De Ning, Xia Cao, Xin Zhang, Gerhard Schumacher, Martin Winter, Elie Paillard, Jie Li, *"P3 $Na_{0.9}Ni_{0.5}Mn_{0.5}O_2$ Cathode Material for Sodium Ion Batteries"*, **Chemistry of Materials** 31(15) (2019) 5376-5383. https://doi.org/10.1021/acs.chemmater.8b03270.

46. Nebil A. Katcho, Javier Carrasco, Damien Saurel, Elena Gonzalo, Man Han, Frederic Aguesse, Teofilo Rojo, *"Origins of Bistability and Na Ion Mobility Difference in P2- and O3-$Na_{2/3}Fe_{2/3}Mn_{1/3}O_2$ Cathode Polymorphs"*, **Advanced Energy Materials** 7(1) (2017) 1601477. https://doi.org/10.1002/aenm.201601477.

47. Elahe Talaie, Victor Duffort, Hillary L. Smith, Brent Fultz, Linda F. Nazar, *"Structure of the high voltage phase of layered P2-$Na_{2/3-z}[Mn_{1/2}Fe_{1/2}]O_2$ and the positive effect of Ni substitution on its stability"*, **Energy & Environmental Science** 8(8) (2015) 2512-2523. https://doi.org/10.1039/C5EE01365H.

48. Junyi Dai, Jiahao Li, Yu Yao, Yan-Ru Wang, Mingze Ma, Ruilin Bai, Yinbo Zhu, Xianhong Rui, Hengan Wu, Yan Yu, *"Strengthening Transition Metal–Oxygen Interaction in Layered Oxide Cathodes for Stable Sodium-Ion Batteries"*, **ACS Nano** 19(11) (2025) 11197-11209. https://doi.org/10.1021/acsnano.4c18526.

49. Zhigao Chen, Yuyu Deng, Ji Kong, Weibin Fu, Chenyang Liu, Ting Jin, Lifang Jiao, *"Toward the High-Voltage Stability of Layered Oxide Cathodes for Sodium-Ion Batteries: Challenges, Progress, and Perspectives"*, **Advanced Materials** 36(26) (2024) 2402008. https://doi.org/10.1002/adma.202402008.

50. W. Weppner, R. A. Huggins, *"Determination of the Kinetic Parameters of Mixed-Conducting Electrodes and Application to the System Li_3Sb"*, **Journal of the Electrochemical Society** 124(10) (1977) 1569. https://doi.org/10.1149/1.2133112.

51. Shinichi Komaba, Naoaki Yabuuchi, Tetsuri Nakayama, Atsushi Ogata, Toru Ishikawa, Izumi Nakai, *"Study on the Reversible Electrode Reaction of $Na_{1-x}Ni_{0.5}Mn_{0.5}O_2$ for a Rechargeable Sodium-Ion Battery"*, **Inorganic Chemistry** 51(11) (2012) 6211-6220. https://doi.org/10.1021/ic300357d.

52. Zheng-Xiao Li, Yi-Meng Wu, Jun-Wei Yin, Peng-Fei Wang, Zong-Lin Liu, Yan-Xuan Wen, Jun-Hong Zhang, Yan-Rong Zhu, Ting-Feng Yi, *"Emerging modification strategies for layered Fe-based oxide cathodes toward high-performance sodium-ion batteries"*, **Journal of Energy Chemistry** 107 (2025) 122-147. https://doi.org/10.1016/j.jechem.2025.03.027.

53. Xin-Yu Liu, Shi Li, Yan-Fang Zhu, Xin-Yu Zhang, Yu Su, Meng-Ying Li, Hong-Wei Li, Bing-Bing Chen, Yi-Feng Liu, Yao Xiao, *"Promoting Layered Oxide Cathodes Based on Structural Reconstruction for Sodium-Ion Batteries: Reversible Phase Transition, Stable Interface Regulation, and Multifunctional Intergrowth Structure"*, **Advanced Functional Materials** 35(4) (2025) 2414130. https://doi.org/10.1002/adfm.202414130.

54. Bohang Song, Enyuan Hu, Jue Liu, Yiman Zhang, Xiao-Qing Yang, Jagjit Nanda, Ashfia Huq, Katharine Page, *"A novel P3-type $Na_{2/3}Mg_{1/3}Mn_{2/3}O_2$ as high capacity sodium-ion cathode using reversible oxygen redox"*, **Journal of Materials Chemistry A** 7(4) (2019) 1491-1498. https://doi.org/10.1039/C8TA09422E.

55. Jae Hyeon Jo, Hee Jae Kim, Ji Ung Choi, Natalia Voronina, Kug-Seung Lee, Kyuwook Ihm, Han-Koo Lee, Hee-Dae Lim, Hyungseok Kim, Hun-Gi Jung, Kyung Yoon Chung, Hitoshi Yashiro, Seung-Taek Myung, *"Facilitating sustainable oxygen-redox chemistry for P3-type cathode materials for sodium-ion batteries"*, **Energy Storage Materials** 46 (2022) 329-343. https://doi.org/10.1016/j.ensm.2022.01.028.

56. M. Yoncheva, R. Stoyanova, E. Zhecheva, E. Kuzmanova, M. Sendova-Vassileva, D. Nihtianova, D. Carlier, M. Guignard, C. Delmas, *"Structure and reversible lithium*

intercalation in a new P'3-phase: $Na_{2/3}Mn_{1-y}Fe_yO_2$ (y = 0, 1/3, 2/3)", **Journal of Materials Chemistry** 22(44) (2012) 23418-23427. https://doi.org/10.1039/C2JM35203F.

57. Xiaohui Rong, Enyuan Hu, Yaxiang Lu, Fanqi Meng, Chenglong Zhao, Xuelong Wang, Qinghua Zhang, Xiqian Yu, Lin Gu, Yong-Sheng Hu, Hong Li, Xuejie Huang, Xiao-Qing Yang, Claude Delmas, Liquan Chen, *"Anionic Redox Reaction-Induced High-Capacity and Low-Strain Cathode with Suppressed Phase Transition"*, **Joule** 3(2) (2019) 503-517. https://doi.org/10.1016/j.joule.2018.10.022.

58. Wei Zheng, Gemeng Liang, Shilin Zhang, Kenneth Davey, Zaiping Guo, *"Understanding voltage hysteresis and decay during anionic redox reaction in layered transition metal oxide cathodes: A critical review"*, **Nano Research** 16(3) (2023) 3766-3780. https://doi.org/10.1007/s12274-022-5003-1.

59. Tengfei Song, Yongxiu Chen, Lin Chen, Emma Kendrick, *"Areal capacity balance to maximize the lifetime of layered oxide/hard carbon sodium-ion batteries"*, **Journal of Power Sources** 624 (2024) 235599. https://doi.org/10.1016/j.jpowsour.2024.235599.

[Supplementary Material]

Compositional Tuning of Fe/Mn and Fe/Ni Ratios in P3-Type Cathodes Enables High Energy Density Sodium-Ion Batteries

Samriddhi Saxena[a], Neha Dagar[a], Velaga Srihari[b], Karthik Chinnathambi[c], Asish Kumar Das[a], Pratiksha Gami[a], Sonia Deswal[d], Pradeep Kumar[d], Himanshu Kumar Poswal[b], Sunil Kumar[a,*]

[a] *Department of Metallurgical Engineering and Materials Science, Indian Institute of Technology Indore, Simrol, 453552, India*

[b] *High Pressure & Synchrotron Radiation Physics Division, Bhabha Atomic Research Centre, Mumbai 400085, India*

[c] *Micron School of Materials Science and Engineering, Boise State University, Boise, ID 83725, USA*

[d] *School of Physical Sciences, Indian Institute of Technology Mandi, Mandi, 175005, India*

[*] *E-mail: sunil@iiti.ac.in*

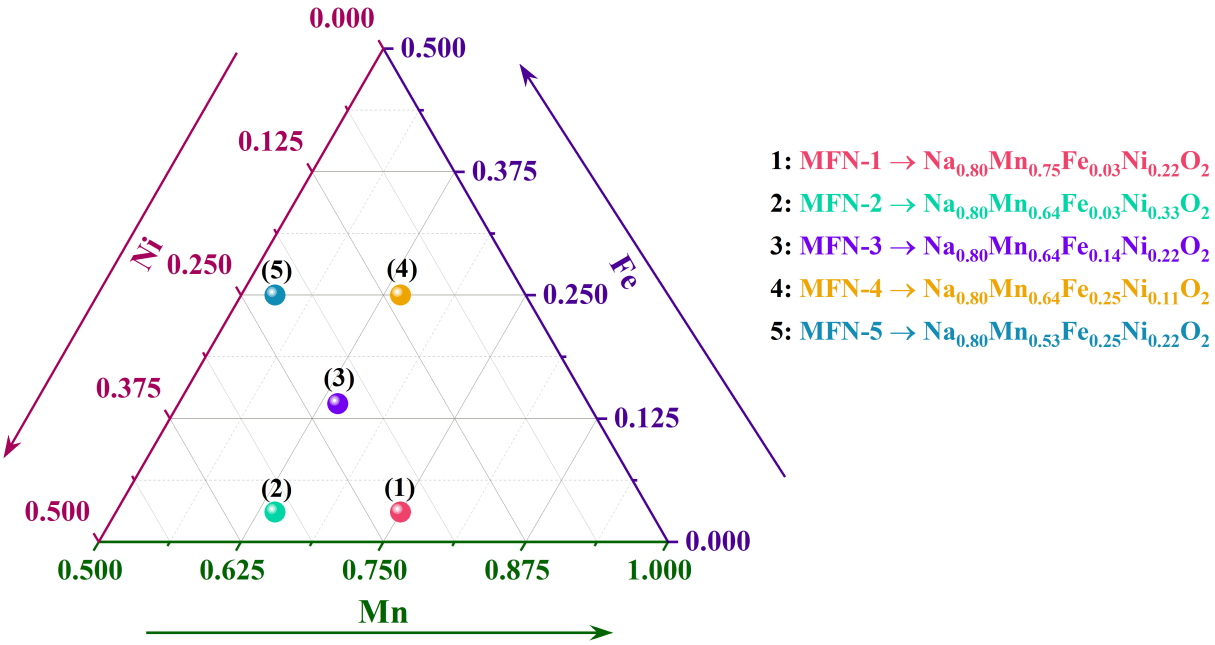

Fig. S1. Compositions selected to represent variations along Fe/Mn and Fe/Ni ratio lines and their abbreviations.

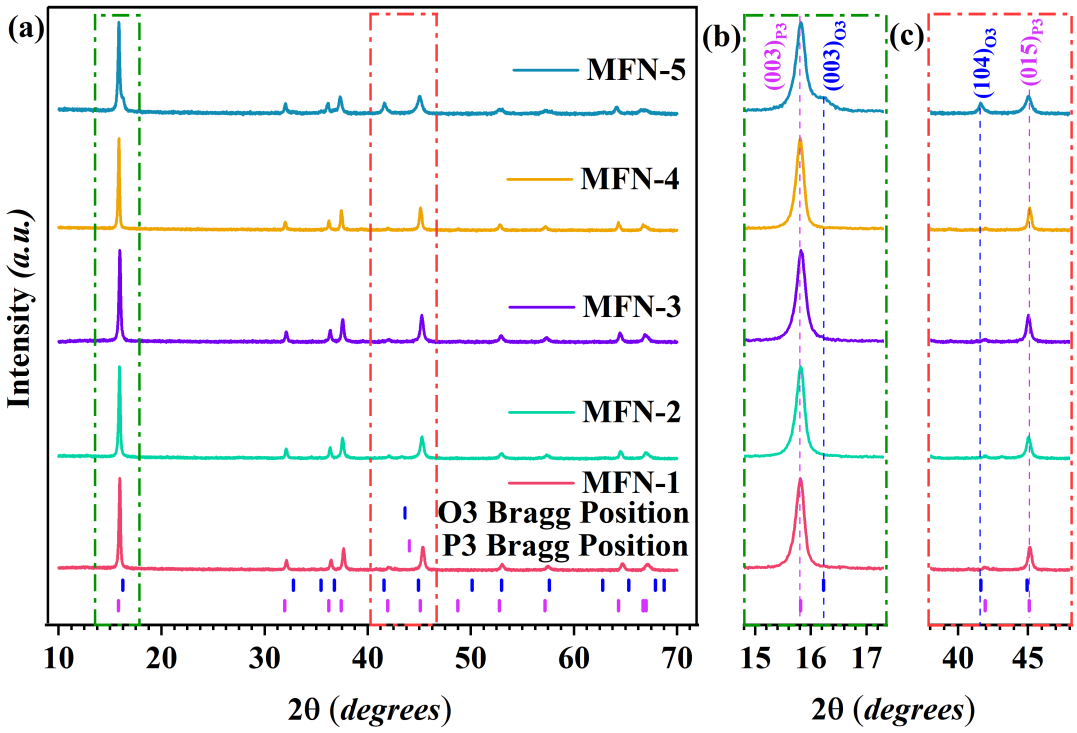

Fig. S2. (a) XRD patterns of the MFN samples calcined at 650 °C, (b) Magnified view of P3(003) & O3(003) peaks, and (c) O3(104) & P3(015) peaks.

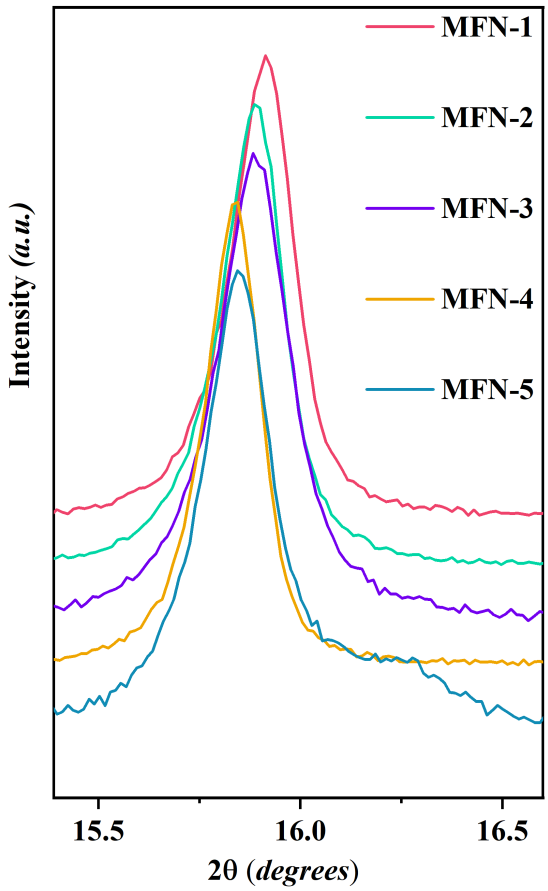

Fig. S3. Comparison of the (003) peak positions of different MFN samples.

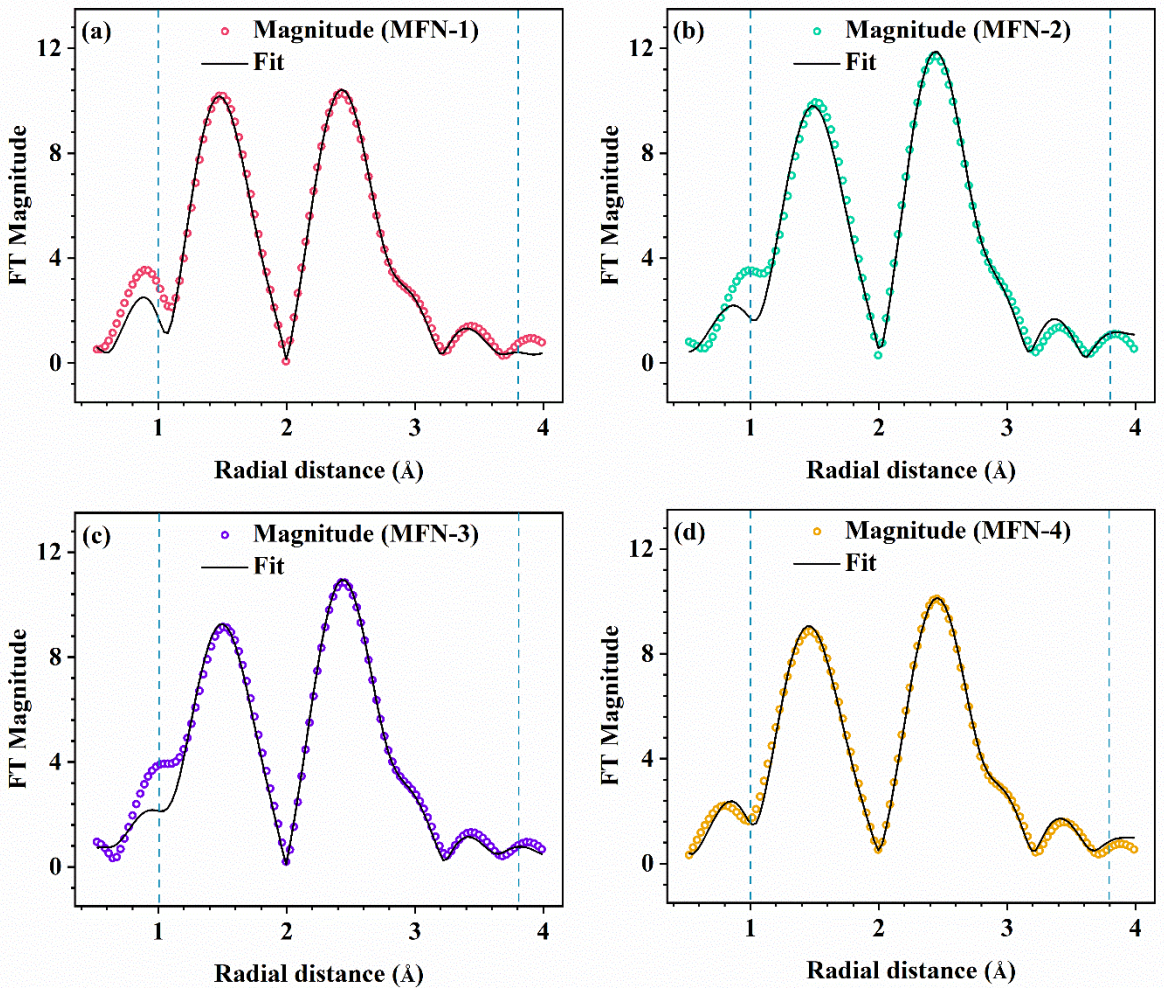

Fig. S4. Fourier transformation of the EXAFS spectra along with the fitting profiles (fitting range of 1–3.8 Å) of (a) MFN-1, (b) MFN-2, (c) MFN-3, and (d) MFN-4 at the Mn K-edge.

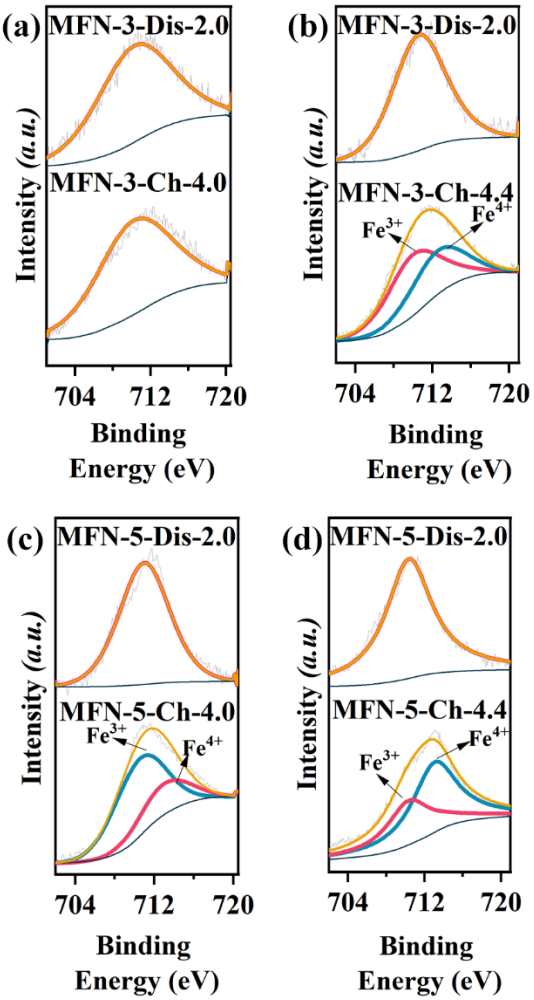

Fig. S5. *Ex situ* XPS Fe 2p spectra of (a) MFN-3 charged to 4.0 V (MFN-3-Ch-4.0) and discharged to 2.0 V (MFN-3-Dis-2.0), (b) MFN-3 charged to 4.4 V (MFN-3-Ch-4.4) and discharged to 2.0 V (MFN-3-Dis-2.0), (c) MFN-5 charged to 4.0 V (MFN-5-Ch-4.0) and discharged to 2.0 V, (MFN-5-Dis-2.0), and (d) MFN-5 charged to 4.4 V (MFN-5-Ch-4.4) and discharged to 2.0 V (MFN-5-Dis-2.0).

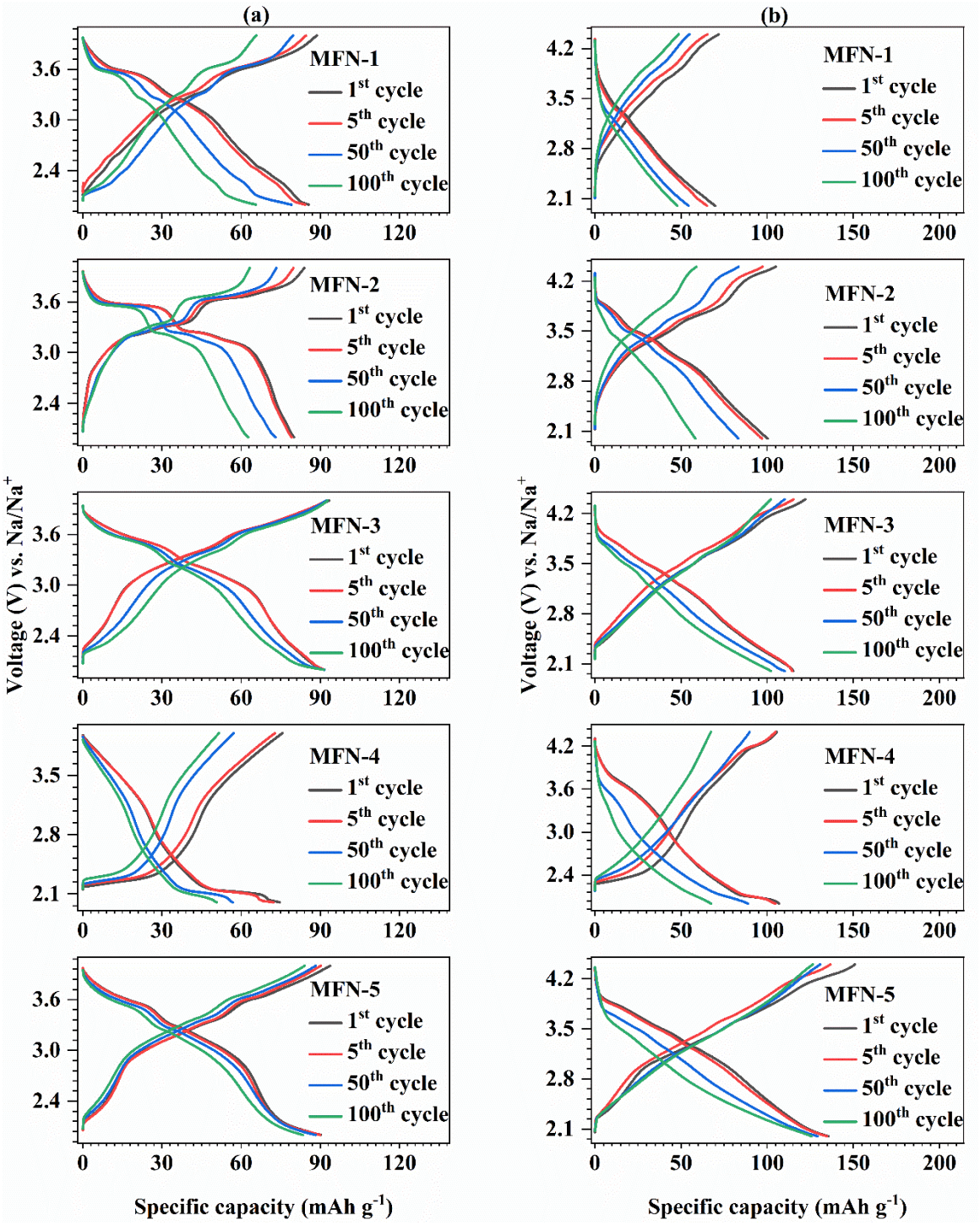

Fig. S6. GCD curves of the 1st, 5th, 50th, and 100th cycles for MFN samples in the (a) 2.0 – 4.0 V and (b) 2.0 – 4.4 V ranges.

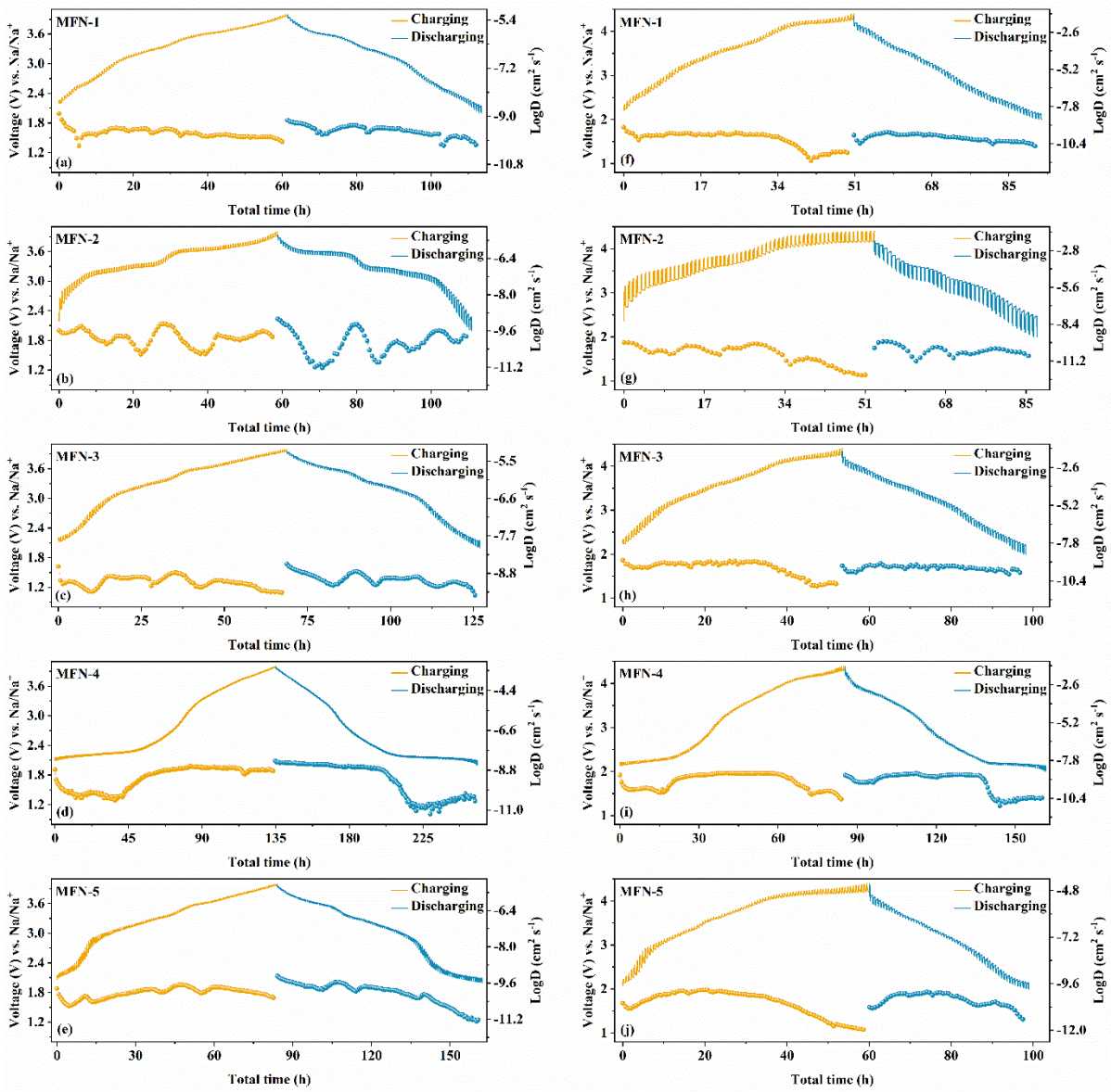

Fig. S7. GITT profiles of MFN samples at 0.1C along with the variations in diffusion coefficients during charge-discharge in the (a-e) 2.0 – 4.0 V and (f-g) 2.0 – 4.4 V ranges.

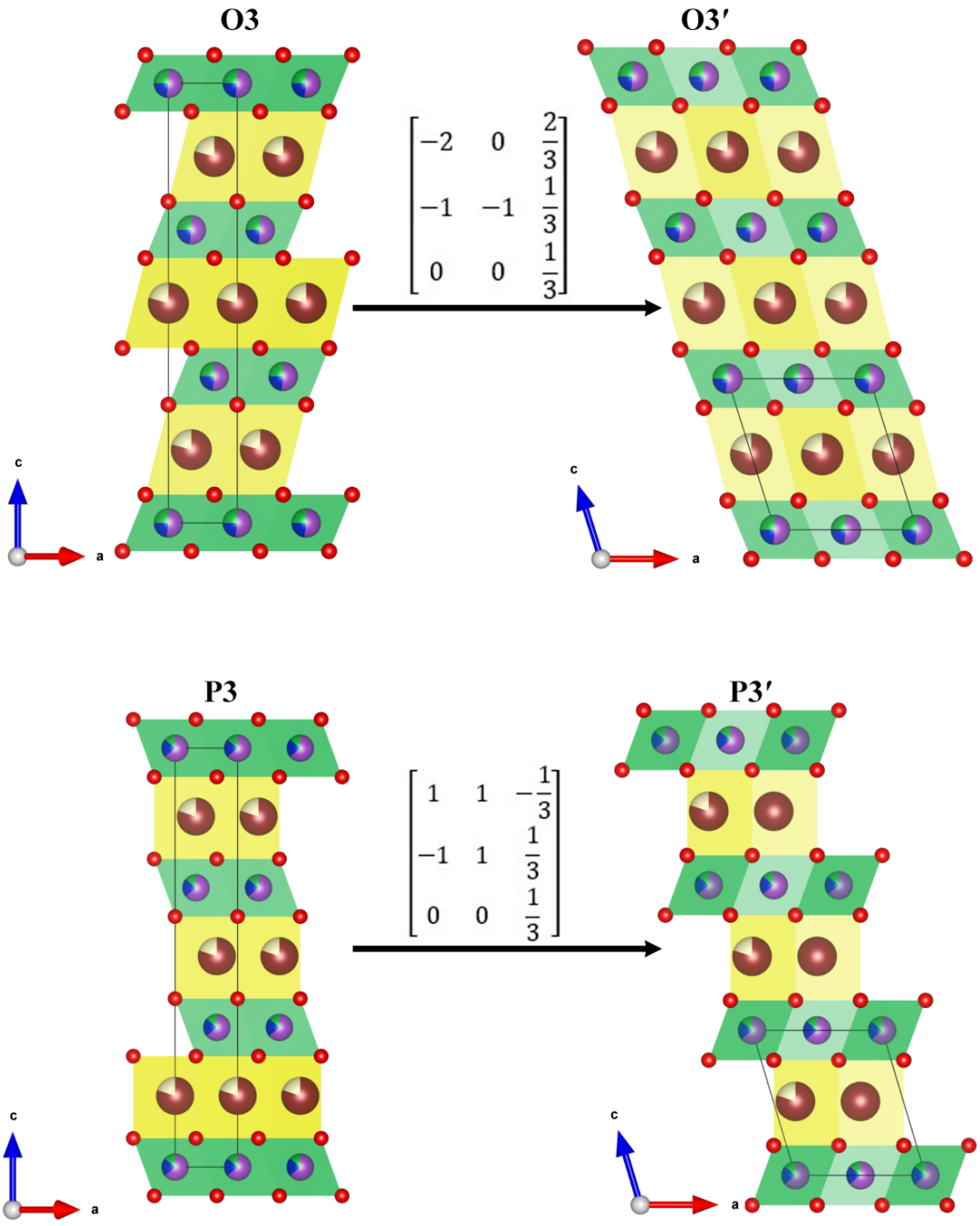

Fig. S8. Monoclinic distortions of the O3 (O3') and P3 (P3') phases.

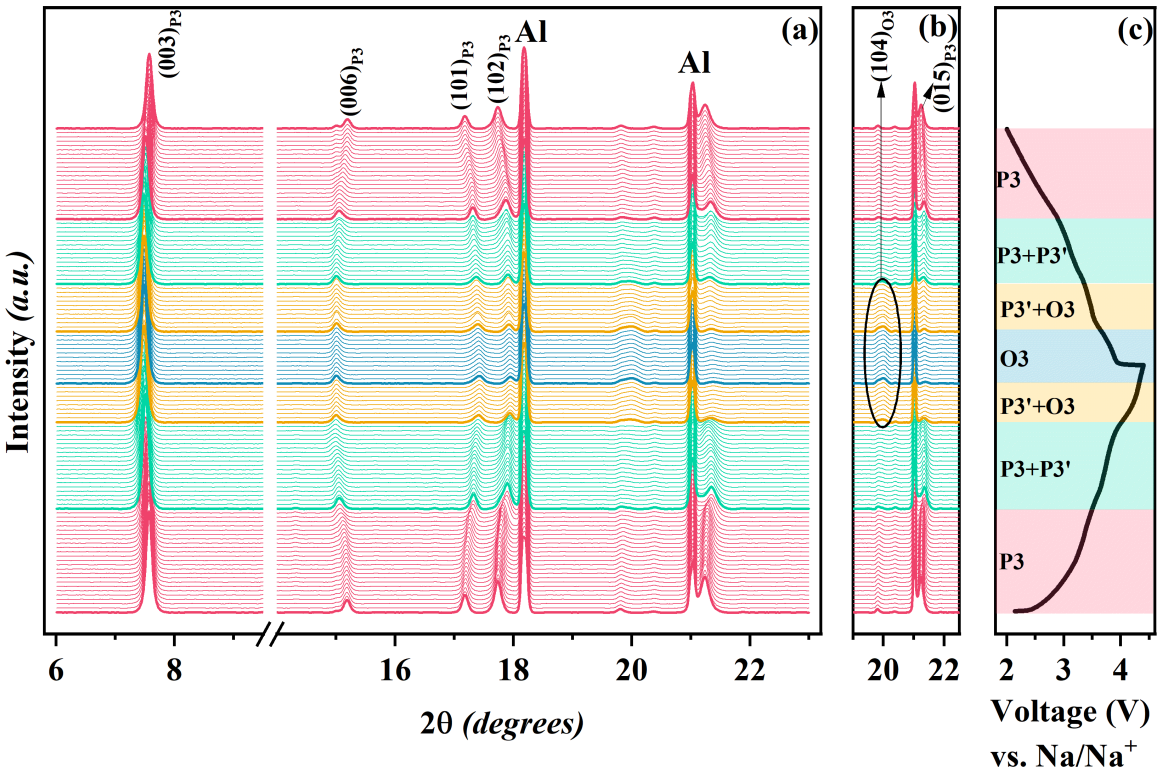

Fig. S9. (a) *Operando* Synchrotron XRD of MFN-2. Magnified view of (b) (104)O3 & (015)P3 peaks of MFN-2 showing various phase transformations in the material. (c) Corresponding GCD curve showing various states of charge/discharge.

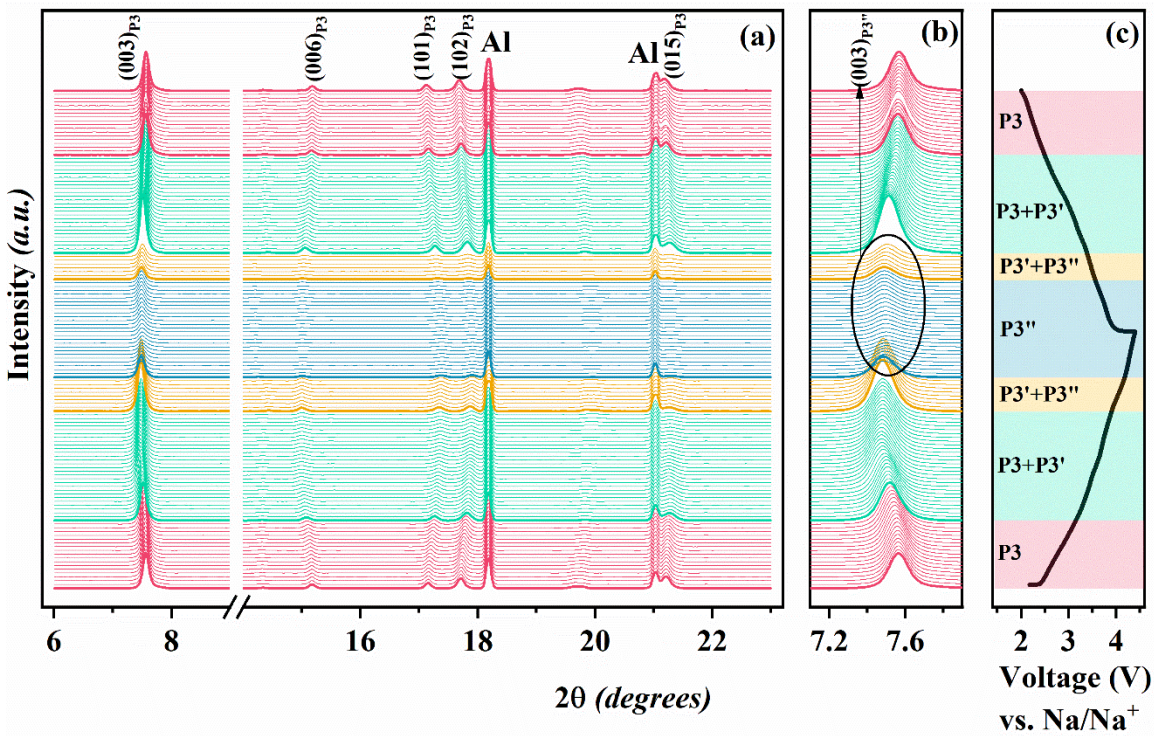

Fig. S10. (a) *Operando* Synchrotron XRD of MFN-3. Magnified view of (b) (003)P3 peak of MFN-3 showing various phase transformations in the material. (c) Corresponding GCD curve showing various states of charge/discharge.

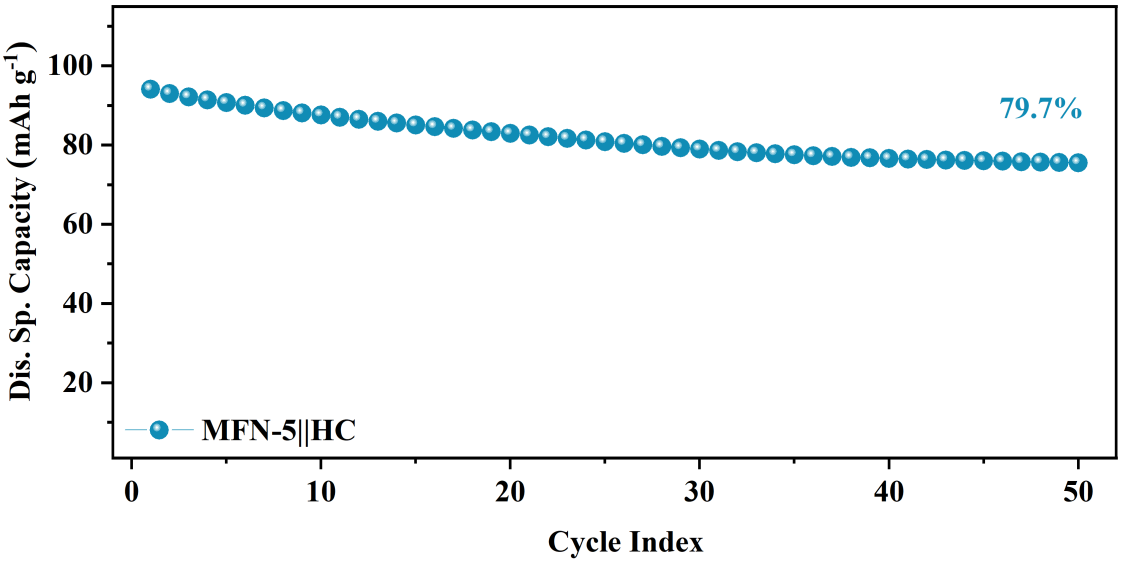

Fig. S11. Full-cell cycling performance of MFN-5 in the 1.0 – 4.2 V range.

Table S1. The chemical compositions of the as-prepared samples estimated by inductively coupled plasma optical emission spectroscopy (ICP-OES).

Sample	***Nominal composition***	***Estimated compositions***
	Na/ Mn/ Fe/ Ni	**Na/ Mn/ Fe/ Ni**
MFN-1	0.8/0.75/0.03/0.22	0.805/0.746/0.028/0.219
MFN-2	0.8/0.64/0.03/0.33	0.798/0.642/0.026/0.331
MFN-3	0.8/0.64/0.14/0.22	0.799/0.639/0.145/0.223
MFN-4	0.8/0.64/0.25/0.11	0.803/0.637/0.248/0.109
MFN-5	0.8/0.53/0.25/0.22	0.802/0.526/0.252/0.217

Tables S2-S6. Crystallographic parameters of MFN samples obtained from Rietveld refinement of room temperature XRD data.

S2: MFN-1

P3 (Space Group: R3m)					
Atom	**x**	**y**	**z**	**Occupancy**	**Site**
Na	0	0	0.171 ± 0.005	0.80	3a
Mn/Fe/Ni	0	0	0	0.75/0.22/0.03	3a
O1	0	0	0.401 ± 0.003	1	3a
O2	0	0	0.599 ± 0.003	1	3a

S3: MFN-2

P3 (Space Group: R3m)					
Atom	**x**	**y**	**z**	**Occupancy**	**Site**
Na	0	0	0.170 ± 0.005	0.80	3a
Mn/Fe/Ni	0	0	0	0.64/0.33/0.03	3a
O1	0	0	0.401 ± 0.002	1	3a
O2	0	0	0.599 ± 0.002	1	3a

S4: MFN-3

P3 (Space Group: R3m)					
Atom	**x**	**y**	**z**	**Occupancy**	**Site**
Na	0	0	0.170 ± 0.007	0.80	3a
Mn/Fe/Ni	0	0	0	0.64/0.22/0.14	3a
O1	0	0	0.399 ± 0.002	1	3a
O2	0	0	0.601 ± 0.002	1	3a

S5: MFN-4

P3 (Space Group: R3m)					
Atom	**x**	**y**	**z**	**Occupancy**	**Site**
Na	0	0	0.171 ± 0.006	0.80	3a
Mn/Fe/Ni	0	0	0	0.64/0.11/0.25	3a
O1	0	0	0.399 ± 0.002	1	3a
O2	0	0	0.601 ± 0.002	1	3a

S6: MFN-5

P3 (Space Group: R3m)					
Atom	**x**	**y**	**z**	**Occupancy**	**Site**
Na	0	0	0.172 ± 0.004	0.80	3a
Mn/Fe/Ni	0	0	0	0.53/0.22/0.25	3a
O1	0	0	0.398 ± 0.003	1	3a
O2	0	0	0.602 ± 0.003	1	3a
O3 (Space Group: $R\bar{3}m$)					
Atom	**x**	**y**	**z**	**Occupancy**	**Site**
Na1	0	0	½	0.80	3b
Mn/Fe/Ni	0	0	0	0.53/0.22/0.25	3a
O	0	0	0.26 ± 0.01	1	6c

Table S7. Transition metal layer and sodium layer spacings in the P3 and O3 phases calculated from the refinement data

Sample	***Phase***	$S_{TM\text{-}O2}$ **(Å)**	$S_{Na\text{-}O2}$ **(Å)**
MFN-1	P3	2.2694	3.3203
MFN-2	P3	2.2696	3.3206
MFN-3	P3	2.2049	3.3914
MFN-4	P3	2.2073	3.3950
MFN-5	P3	2.1713	3.4280
	O3	2.1068	3.3512

Table S8. Mn^{3+}/Mn^{4+} ratios for the MFN samples, obtained by fitting of the Mn 2p XPS spectra

Sample	Mn^{3+}: Mn^{4+}
MFN-1	45:55
MFN-2	17:83
MFN-3	34:66
MFN-4	52:48
MFN-5	21:79

Table S9. The range of diffusion coefficients of MFN samples.

Sample	***Diffusion coefficient*** (D_{Na+}) $(cm^2\ s^{-1})$ ***2.0 – 4.0 V range***	***Diffusion coefficient*** (D_{Na+}) $(cm^2\ s^{-1})$ ***2.0 – 4.4 V range***
MFN-1	$7.99 \times 10^{-11} – 1.28 \times 10^{-9}$	$2.63 \times 10^{-12} – 5.79\ 10^{-10}$
MFN-2	$5.85 \times 10^{-12} – 8.45 \times 10^{-10}$	$5.16 \times 10^{-13} – 1.88\ 10^{-10}$
MFN-3	$3.59 \times 10^{-10} – 2.97\ 10^{-9}$	$1.72 \times 10^{-11} – 1.04\ 10^{-9}$
MFN-4	$5.99 \times 10^{-12} – 5.07 \times 10^{-9}$	$9.85 \times 10^{-12} – 2.14 \times 10^{-9}$
MFN-5	$4.02 \times 10^{-12} – 4.07 \times 10^{-10}$	$2.46 \times 10^{-11} – 1.19 \times 10^{-9}$

Table S10. The lattice parameters of various phases in MFN-5 during charge-discharge.

Voltage	***Space group***	***a (Å)***	***b (Å)***	***c (Å)***	***β (°)***
Ch. – 2.1 V	*R*3*m*	2.8875 ± 0.0002	2.8875 ± 0.0002	16.810 ± 0.003	0
	$R\bar{3}m$	2.9461 ± 0.0003	2.9461 ± 0.0003	16.355 ± 0.004	0
Ch. – 3.0 V	*R*3*m*	2.8820 ± 0.0002	2.8820 ± 0.0002	16.816 ± 0.003	0
	*C*2/*m*	4.997 ± 0.002	2.928 ± 0.002	5.98 ± 0.05	110.5 ± 0.5
Ch. – 3.5 V	*R*3*m*	2.8690 ± 0.0002	2.8690 ± 0.0002	16.829 ± 0.002	0
	*C*2/*m*	4.964 ± 0.001	2.733 ± 0.004	6.13 ± 0.01	110.0 ± 0.2
Ch. – 3.8 V	*C*2/*m*	4.869 ± 0.003	2.720 ± 0.003	6.20 ± 0.01	109.5 ± 0.2
	$R\bar{3}m$	2.8656 ± 0.0005	2.8656 ± 0.0005	16.843 ± 0.001	0
Ch. – 4.1 V	$R\bar{3}m$ (P3”)	2.8489 ± 0.0004	2.8489 ± 0.0004	16.889 ± 0.002	0
	$R\bar{3}m$ (O3)	2.865 ± 0.001	2.865 ± 0.001	16.127 ± 0.004	0
Ch. – 4.4 V	$R\bar{3}m$ (P3”)	2.8485 ± 0.0007	2.8485 ± 0.0007	16.934 ± 0.001	0
	$R\bar{3}m$ (O3)	2.857 ± 0.002	2.857 ± 0.002	15.98 ± 0.01	0

Dis. – 3.6 V	$R\bar{3}m$ (P3")	2.8492 ± 0.0006	2.8492 ± 0.0006	16.9310 ± 0.0006	0
	$R\bar{3}m$ (O3)	2.866 ± 0.002	2.866 ± 0.002	16.06 ± 0.02	0
Dis. – 3.3 V	*C2/m*	4.890 ± 0.001	2.708 ± 0.002	6.241 ± 0.003	108.1 ± 0.1
	R3m	2.875 ± 0.001	2.875 ± 0.001	16.921 ± 0.005	0
Dis. – 2.9 V	*R3m*	2.8874 ± 0.0006	2.8874 ± 0.0006	16.848 ± 0.003	0
	C2/m	5.012 ± 0.003	2.843 ± 0.004	6.17 ± 0.01	110.6 ± 0.3
Dis. – 2.3 V	*R3m*	2.892 ± 0.001	2.892 ± 0.001	16.814 ± 0.001	0
	$R\bar{3}m$	2.889 ± 0.006	2.889 ± 0.006	16.15 ± 0.06	0
Dis. – 2.0 V	*R3m*	2.899 ± 0.001	2.899 ± 0.001	16.76 ± 0.01	0
	$R\bar{3}m$	2.944 ± 0.001	2.944 ± 0.001	16.27 ± 0.01	0

Table S11. The lattice parameters of various phases in MFN-2 during charge-discharge.

Voltage	***Space group***	***a (Å)***	***b (Å)***	***c (Å)***	***β (°)***
Ch. – 2.1 V	*R*3*m*	2.8884 ± 0.0003	2.8884 ± 0.0003	16.775 ± 0.003	0
Ch. – 3.5 V	*R*3*m*	2.8781 ± 0.0003	2.8781 ± 0.0003	16.794 ± 0.001	0
Ch. – 3.7 V	*R*3*m*	2.8560 ± 0.0001	2.8560 ± 0.0001	16.852 ± 0.002	0
	*C*2/*m*	5.081 ± 0.003	2.707 ± 0.005	6.17 ± 0.01	110.8 ± 0.3
Ch. – 4.0 V	*R*3*m*	2.8540 ± 0.0001	2.8540 ± 0.0001	16.885 ± 0.002	0
	*C*2/*m*	5.025 ± 0.004	2.700 ± 0.006	6.18 ± 0.02	108.2 ± 0.4
Ch. – 4.3 V	*C*2/*m*	5.020 ± 0.004	2.688 ± 0.002	6.236 ± 0.003	106.7 ± 0.1
	$R\bar{3}m$	2.8481 ± 0.0004	2.8481 ± 0.0004	16.982 ± 0.003	0
Ch. – 4.4 V	$R\bar{3}m$	2.8466 ± 0.0003	2.8466 ± 0.0003	17.016 ± 0.001	0
Dis. – 3.9 V	$R\bar{3}m$	2.8475 ± 0.0003	2.8475 ± 0.0003	17.011 ± 0.001	0
Dis. – 3.6 V	$R\bar{3}m$	2.8523 ± 0.0004	2.8523 ± 0.0004	16.988 ± 0.004	0
	*C*2/*m*	5.0263 ± 0.0004	2.692 ± 0.001	6.2492 ± 0.0005	106.9 ± 0.1

Dis. – 3.3 V	*C*2/*m*	5.070 ± 0.005	2.702 ± 0.001	6.16 ± 0.03	108.7 ± 0.7
	*R*3*m*	2.8560 ± 0.0002	2.8560 ± 0.0002	16.887 ± 0.001	0
Dis. – 3.1 V	*C*2/*m*	5.086 ± 0.006	2.703 ± 0.002	6.15 ± 0.03	110.1 ± 0.8
	*R*3*m*	2.8562 ± 0.0002	2.8562 ± 0.0002	16.881 ± 0.004	0
Dis. – 2.9 V	*C*2/*m*	5.104 ± 0.007	2.71 ± 0.02	6.12 ± 0.03	110.5 ± 0.4
	*R*3*m*	2.8595 ± 0.0002	2.8595 ± 0.0002	16.858 ± 0.003	0
Dis. – 2.4 V	*R*3*m*	2.8702 ± 0.0001	2.8702 ± 0.0001	16.807 ± 0.001	0
Dis. – 2.0 V	*R*3*m*	2.8879 ± 0.0001	2.8879 ± 0.0001	16.766 ± 0.002	0

Table S12. The lattice parameters of various phases in MFN-3 during charge-discharge.

Voltage	***Space group***	***a (Å)***	***b (Å)***	***c (Å)***	***β (°)***
Ch. – 2.1 V	*R*3*m*	2.8902 ± 0.0003	2.8902 ± 0.0003	16.788 ± 0.004	0
Ch. – 3.1 V	*R*3*m*	2.8834 ± 0.0001	2.8834 ± 0.0001	16.796 ± 0.001	0
Ch. – 3.6 V	*R*3*m*	2.8693 ± 0.0001	2.8693 ± 0.0001	16.839 ± 0.001	0
	*C*2/*m*	5.243 ± 0.006	2.86 ± 0.06	6.21 ± 0.01	110.6 ± 0.3
Ch. – 4.0 V	*R*3*m*	2.8619 ± 0.0001	2.8619 ± 0.0001	16.90 ± 0.01	0
	*C*2/*m*	5.111 ± 0.001	2.706 ± 0.001	6.22 ± 0.03	109.4 ± 0.6
Ch. – 4.2 V	*C*2/*m*	5.07 ± 0.01	2.657 ± 0.001	6.243 ± 0.003	106.8 ± 0.6
	$R\bar{3}m$	2.8586 ± 0.0005	2.8586 ± 0.0005	16.929 ± 0.001	0
Ch. – 4.4 V	$R\bar{3}m$	2.8549 ± 0.0007	2.8549 ± 0.0007	16.941 ± 0.001	0
Dis. – 3.7 V	$R\bar{3}m$	2.860 ± 0.001	2.860 ± 0.001	16.925 ± 0.002	0
Dis. – 3.5 V	$R\bar{3}m$	2.8614 ± 0.0004	2.8614 ± 0.0004	16.910 ± 0.005	0
	*C*2/*m*	5.09 ± 0.02	2.691 ± 0.005	6.351 ± 0.002	107.1 ± 0.1

Dis. – 3.3 V	*R*3*m*	2.8676 ± 0.0002	2.8676 ± 0.0002	16.875 ± 0.002	0
	*C*2/*m*	5.13 ± 0.01	2.709 ± 0.005	6.24 ± 0.06	107.9 ± 0.8
Dis. – 3.0 V	*R*3*m*	2.8779 ± 0.0001	2.8779 ± 0.0001	16.803 ± 0.002	0
	*C*2/*m*	5.15 ± 0.01	2.81 ± 0.06	6.18 ± 0.07	109.3 ± 0.8
Dis. – 2.5 V	*R*3*m*	2.8875 ± 0.0001	2.8875 ± 0.0001	16.760 ± 0.002	0
	*C*2/*m*	5.25 ± 0.01	2.85 ± 0.02	6.14 ± 0.06	110.8 ± 0.5
Dis. – 2.3 V	*R*3*m*	2.8910 ± 0.0001	2.8910 ± 0.0001	16.746 ± 0.002	0
Dis. – 2.0 V	*R*3*m*	2.8931 ± 0.0001	2.8931 ± 0.0001	16.741 ± 0.002	0